



This is a repository copy of *Natural circulation in an enclosed rod bundle of large aspect ratio*.

White Rose Research Online URL for this paper:
<https://eprints.whiterose.ac.uk/176801/>

Version: Accepted Version

Article:

Chinembiri, K., He, S. orcid.org/0000-0003-0326-2447 and Li, J. (2021) Natural circulation in an enclosed rod bundle of large aspect ratio. *Applied Thermal Engineering*, 188. 116534. ISSN 1359-4311

<https://doi.org/10.1016/j.applthermaleng.2020.116534>

Article available under the terms of the CC-BY-NC-ND licence
(<https://creativecommons.org/licenses/by-nc-nd/4.0/>).

Reuse

This article is distributed under the terms of the Creative Commons Attribution-NonCommercial-NoDerivs (CC BY-NC-ND) licence. This licence only allows you to download this work and share it with others as long as you credit the authors, but you can't change the article in any way or use it commercially. More information and the full terms of the licence here: <https://creativecommons.org/licenses/>

Takedown

If you consider content in White Rose Research Online to be in breach of UK law, please notify us by emailing eprints@whiterose.ac.uk including the URL of the record and the reason for the withdrawal request.



eprints@whiterose.ac.uk
<https://eprints.whiterose.ac.uk/>

Natural circulation in an enclosed rod bundle of large aspect ratio

Kenneth Chinembiri^a, Shuisheng He^{a,*}, Jiankang Li^b

^a*Heat, Flow and Turbulence Research Group, Department of Mechanical Engineering, The University of Sheffield, S1 3JD, UK*

^b*Fuel Route Systems Branch, Engineering, EDF Energy Generation, Barnett Way, Barnwood, Gloucester, GL4 3RS, UK*

Abstract

Highly turbulent natural circulation in an enclosed tall rod bundle is investigated using Large Eddy Simulation (LES). The rod bundle consists of 36 heated rods and an insulated central tube, which are enclosed by a cooled containment wall, this geometry is directly relevant to nuclear fuel bundles and generic heat exchangers. For nuclear fuel bundles, natural circulation is of importance in accident scenarios. A 60° azimuthally periodic sector of the bundle is modelled. The Rayleigh number based on the height is 7.6×10^{12} and 1.23×10^{13} for the two cases studied. The flow, turbulence, and thermal characteristics of the system show strong distinct features in the top, middle, and bottom regions (about 0.2, 0.6, and 0.2 splits), which are strongly influenced by the vertically developing buoyancy-driven boundary layer on the containment surface. The flow in the top region is largely stagnant with strong thermal stratification and weak cross flow. A laminar boundary layer is however formed on the containment wall which later transitions to turbulence. This turns out to be the dominant flow feature in the rod bundle. The velocity profile and heat transfer in this top region are well represented, respectively, by a similarity solution for laminar flow and a well-established Nusselt correlation for an unconfined flat plate. In the middle-height region, the flow can be naturally split into an outer flow and a central flow zone. The former resembles the flow in a simple, rectangular, asymmetrically heated/cooled cavity, and the heat transfer to the containment is well represented by a turbulent natural convection correlation. The central flow zone largely re-

sembles mixed convection in a heated upwards pipe/channel flow, though the entrainment of fluid from the outer zone means that the flow accelerates axially until the middle-height. Irrespective of the differences in the two zones, the near-wall behaviour of the flow and thermal fields on the rods and containment wall shows a strong similarity at different heights as well as between the two zones. They are also shown to be consistent with buoyancy-driven flows in simple geometries. In the bottom region, the flow is dominated by an impinging jet from the containment wall and a resultant cross flow from the outer zone to the inner one.

Keywords: Natural convection, Rod bundle, Enclosed cavity, Buoyancy

1. Introduction

Investigations to date for natural circulation flows have mostly been on laminar flow and/or simple cavities (rectangular or annular). However, in an industrial setting, the flow is usually highly turbulent with complex geometry. This paper aims to add to the general body of knowledge by studying thermal-hydraulics in the more complex configuration of a sealed rod bundle.

Elder[1] experimentally investigated turbulent natural convection in rectangular cavities with aspect ratios ranging from 1 - 60. At Rayleigh numbers (Ra_L) greater than 10^7 , the system transitioned to turbulence. The formation of the boundary layer was described as similar to that for an isolated vertical plate. However, the critical Rayleigh number was found to be aspect ratio dependant. Yin et al.[2] and MacGregor and Emery[3] both similarly concluded, the aspect ratio influenced the critical Rayleigh number.

Nomenclature

Greek letters

* Corresponding author: s.he@sheffield.ac.uk

- α thermal diffusivity, $\lambda / \rho C_p$ [m^2/s]
- 15 β thermal expansion coefficient, $1/(T + 273.15)$ [$1/^\circ C$]
- ΔT_H Horizontal temperature difference
- ΔT_V Vertical temperature difference
- $\Delta x^+, \Delta y^+, \Delta z^+$ grid spacing
- δ_{ij} Kronecker delta
- 20 λ thermal conductivity, [$W/m^\circ C$]
- μ molecular viscosity, [$Pa \cdot s$]
- ρ density, [kg/m^3]

Roman Letters

- A aspect ratio, H/L
- 25 Cf Fanning friction factor, $\tau_w / \rho (\bar{w}^2 / 2)$
- Cp specific heat capacity, [$J/kg^\circ C$]
- $Gr_{\Delta T}$ Grashof number, $g\beta (T_w - T) L^3 / (v^2)$
- $Gr_{q''}$ Grashof number, $g\beta q'' L^4 / (v^2 \lambda)$
- H Height, [m]
- 30 Nu Nusselt number, hL / λ
- Pr Prandtl number, $\mu C_p / \lambda$
- Ra Rayleigh number, $GrPr$
- D diameter, [m]
- g gravity, [m/s^2]

35	h	heat transfer coefficient, $[\text{W}/(\text{m}^2\text{°C})]$
	k	turbulent kinetic energy, $[\text{m}^2/\text{s}^2]$
	L	length scale, $[\text{m}]$
	p/d	pitch-to-diameter ratio
	q''	heat flux, $[\text{W}/\text{m}^2]$
40	R	radius, $[\text{m}]$
	r	radial distance, $[\text{m}]$
	T	temperature, $[\text{°C}]$
	t	time, $[\text{s}]$
	T^*	non-dimensional temperature
45	T^+	non-dimensional temperature normalised using friction temperature
	u, v, w	velocity components, $[\text{m}/\text{s}]$
	u^+, v^+, w^+	non-dimensional velocity normalised using friction velocity
	V	reference velocity, $[\text{m}/\text{s}]$
	ν	kinematic viscosity, μ/ρ $[\text{m}^2/\text{s}]$
50	w_τ	friction velocity, $\sqrt{\tau_w/\rho}$ $[\text{m}/\text{s}]$
	x, y, z	spatial distances, $[\text{m}]$
	y^+	non-dimensional distance in viscous units, $y^+ = y\bar{w}_\tau/\nu$
	Z^*	non-dimensional height

Subscripts

55	c	cold surface
----	-----	--------------

crs cross flow

h hot surface

i, j, k directional terms

max maximum velocity

60 *num - diff* numerical diffusion

sgs sub-grid scale

w wall

Betts and Bokhari[4] carried out experimental measurements in a tall rectangular enclosure. The aspect ratio of the cavity was 28.6 with a Rayleigh number of 10^6 . In the turbulent region, the hot and cold boundary layers strongly interacted with each other. This leads to peak velocity fluctuations occurring in the core of the cavity. Velocity and temperature profiles also had a linear gradient across the core. This is contrary to the distributions observed for low aspect ratio cavities. Cheesewright[5] studied a cavity with an aspect ratio of 5 and at the core, the flow was quiescent with uniform temperature. Other investigators have made similar observations[6, 3, 7].

70 Barhaghi and Davidson[6] used coarse DNS and LES to study, the natural convection boundary layer in a sealed-tall cavity with an aspect ratio of 5. In their LES computations, the dynamic, Smagorinsky and WALE models were tested. The authors further considered the influence of the grid resolution on the obtained results, by refining the streamwise and spanwise mesh resolutions by a factor of two for the LES computations. In the wall-normal direction the grid was maintained at 98 divisions with a given y^+ value of ≈ 0.6 . Results obtained suggested the convective grid resolutions used in forced flows were not appropriate for use in natural convective flows. In particular, the authors noted within the transition region the accuracy of the solution was highly grid dependant. While in the turbulent region the solution was indifferent to the grid resolution. The

authors also noted the onset of transition was predicted at different locations by the various sub-
80 grid models, with the authors contending transition onset was better predicted using the Dynamic
model. Kizldarg et al.[8] investigated the onset of transition in a water-filled cavity with a Prandtl
number of 4.31 and an aspect ratio of 5. They compared several sub-grid models against DNS
data. In their comparison they found the WALE model to perform better than the other models
tested with excellent comparisons against the DNS data.

85 The next portion of the literature review looks at buoyancy induced flows in geometries other
than cavities examples would include heated channels, vertical plates, etc.

The natural convection boundary layer on an isolated flat vertical surface was experimentally
studied by Tsuji and Nagano[9]. Contrary to forced convection flows they showed the y^+ range
for the viscous sublayer was much smaller. However, the profile for T^+ against y^+ , showed for the
90 non-dimensional temperature a linear relation existed up to $y^+ \leq 5$, similar to forced convection
flows. In their measurements, the mean heat transfer rate remained constant with height, while the
wall shear stress increased.

Natural convection in an open-ended pipe was one of the test configurations experimentally
investigated by Eckert and Diaguila [10]. The length of the heated pipe section was 2.5 m with an
95 internal diameter of 0.6 m. High Grashof numbers, based on the length, up to 10^{13} were studied
in the experiment. Thin momentum and thermal boundary layers existed on the heated pipe walls.
Heat transfer in the turbulent region was well correlated to that for an isolated flat vertical surface
in a large free space. However, in the laminar region heat transfer was over predicted. Large
diameter pipes were also investigated by Yan and Lin[11], using both experimental and numerical
100 methods. Similarly, they showed heat transfer phenomena was akin to an isolated vertical plate.

Ohk and Chung [12] experimentally and numerically investigated the influence of length, di-
ameter and Prandtl number on natural convective flow through an open-ended pipe. The pipe

length ranged from 0.2 m to 1 m, with the pipe diameter ranging from 0.003 m to 0.03 m. A wide range of Rayleigh numbers was investigated and the peak Grashof number based on length was $\approx 10^{10}$. For large diameter pipes, the observations were consistent with the studies cited in the preceding paragraph [10, 11]. Decreases in the pipe diameter and/or Prandtl number leads to the thermal boundary layers merging and velocity peaks occurring near the centre, which is a deviation from the typical natural convection flow profile. Instead, this is now a mixed convection pipe flow. As the pipe length was increased it was shown the heat flux progressively reduced as the thermal boundary layer developed along the pipe length.

Inagaki and Maruyama[13] investigated laminar, transitional and turbulent natural convection between two uniformly heated parallel vertical plates open at four sides. The effect of various gap spacings and channel length were additional parameters investigated. The working fluid was water and the peak Rayleigh number (based on height) investigated was 10^{15} . In the laminar region heat transfer increased with a decrease in gap spacing. This behaviour was attributed to the chimney effect. However, in the turbulent region with a decrease in gap spacing heat transfer deterioration occurred at Rayleigh numbers greater than 10^{14} . The authors stated this behaviour and the physical mechanisms underlying it was similar to heat transfer deterioration in forced flow vertical channels as a result of buoyancy. Increasing the channel length had the following effects; there was a notable increase in the chimney effect, leading to improved heat transfer in the laminar region. There was also a marked increase on the effect of heat transfer deterioration but at now higher Rayleigh numbers.

Lewandowski et al.[14] experimentally investigated the effect of gap spacing on the computed Nusselt number for a symmetrically heated vertical channel. The working fluid was air with a given Prandtl number of 0.71 and a peak Rayleigh number (based on height) of up to 10^9 . Gap spacing was shown to have a significant effect on the heat transfer rate. At a gap spacing of

approximately zero, the heat transfer was via conduction. As the gap spacing increased, convection became dominant past a critical Rayleigh number. With a further increase in spacing leading to the formation of the chimney effect, which greatly aided the heat transfer. A peak heat transfer enhancement of 69% compared against that for an isolated vertical plate was recorded as a result of these effects. However, further increases in gap spacing led to a weakening of the chimney effect up until the increase in gap space was such that the two convective boundary layers no longer interacted and the predicted heat transfer coefficient approximated to that of a flat vertical plate.

Studies that have investigated rod bundles geometries are given in the next couple of paragraphs. Natural circulation in square rod bundle arrays was experimentally investigated by Keyhani et al.[15]. The test configurations studied consisted of a 3 x 3 and a 5 x 5 rod bundle, with pitch-to-diameter ratios of 3.08 and 2.25, respectively. The characteristic length used was that of the containment diameter (D). For the 3 x 3 bundle, the resulting aspect ratio was $H/D = 10.62$ and the Rayleigh number range was $1.95 \times 10^4 \leq Ra_D \leq 4.5 \times 10^7$. The aspect ratio for the 5 x 5 case was $H/D = 5.79$ and the Rayleigh number range was $2.6 \times 10^5 \leq Ra_D \leq 1.06 \times 10^9$. Three fluids which are helium, air, and water were considered for the 3 x 3 bundle. Their overall Nusselt number correlations for the boundary layer flow regime were $0.072Ra_D^{0.332}$ and $0.151Ra_D^{0.274}$ for helium/air and water, respectively. However, for the 5 x 5 bundle only helium was studied and the Nusselt number correlation is $0.095Ra_D^{0.323}$. A flow visualisation study was also carried out for the 3 x 3 bundle. The containment was switched to one made of acrylic giving an aspect ratio (H/D) of 11.81 and the flow was visualised using suspended aluminium powder in ethylene glycol. The Rayleigh number of the study was $Ra_D = 2.92 \times 10^7$ and the Prandtl number was 46.4. The flow observations showed that there was an upward boundary layer flow regime on the rod surfaces. At the sub-channel centres, between the rods, there was no flow interaction thus the rods behaved as if they were isolated. Interestingly, the authors noted there was a low magnitude downward flow

here. At the end-regions cross flow was observed.

In a related study[16], we investigated a similar rod bundle geometry to that investigated herein but with a short height of 0.25 m. In this configuration, the fluid is stratified and the flow in the sub-channels is stagnant. Natural circulation occurs on the walls and is dominated by the formation and development of a laminar boundary layer on the containment wall. The spread of turbulence from the containment wall had a strong influence on the flow development at the rods.

The review has shown a distinct lack of literature concerning natural circulation in rod bundle type geometries. This paper aims to investigate natural circulation in a rod bundle similar to that studied by Chinembiri et al.[16] but with much larger aspect ratios by increasing the domain height fourfold, thus allowing investigations into fully developed turbulence. In turn, this would feed into the overall aim of providing new knowledge in natural circulation flows in enclosed cavities.

The paper is split into the following sections; Chapter 1 covers the numerical methods, general setup, and details of the various non-dimensional parameters of interest. Chapter 2 details the results obtained from the simulations conducted and the conclusions are given in Chapter 3.

2. Numerical method

Simulations conducted for the present study are carried out using Code_Saturne an open-source solver developed by EDF. Code_Saturne is a finite volume, co-located, and single-phase solver, which is routinely used for nuclear thermal hydraulic problems.

2.1. Governing equations

LES simulations are conducted in this study and the spatially filtered governing equations are given below.

Continuity:

$$\frac{\partial \rho}{\partial t} + \frac{\partial \rho \bar{u}_i}{\partial x_i} = 0 \quad (1)$$

Momentum:

$$\frac{\partial \rho \bar{u}_i}{\partial t} + \frac{\partial}{\partial x_j} (\rho \bar{u}_i \bar{u}_j) = -\frac{\partial \bar{P}}{\partial x_i} + \rho g_i + \mu \frac{\partial}{\partial x_j} \left(\frac{\partial \bar{u}_i}{\partial x_j} + \frac{\partial \bar{u}_j}{\partial x_i} \right) - \frac{\partial \rho \tau_{ij}^r}{\partial x_j} \quad (2)$$

Energy:

$$\rho \left(\frac{\partial \bar{T}}{\partial t} + \frac{\partial \bar{u}_i \bar{T}}{\partial x_i} \right) = \frac{\mu}{\text{Pr}} \frac{\partial^2 \bar{T}}{\partial x_i \partial x_i} - \frac{\partial \rho \Pi_{\text{sgs},i}}{\partial x_i} \quad (3)$$

The large scales are resolved in equations 1 - 3, while the scales smaller than the filter width (sub-grid scales) are modelled. The term τ_{ij}^r represents the sub-grid scale stress tensor, which is closed through the use of a sub-grid model and the eddy viscosity assumption as shown in Equation

175 4:

$$\tau_{ij}^r = -2\nu_{\text{sgs}} \bar{S}_{ij} + \frac{1}{3} \tau_{kk} \delta_{ij} \quad (4)$$

where \bar{S}_{ij} is defined as $\frac{1}{2} \left(\frac{\partial \bar{u}_i}{\partial x_j} + \frac{\partial \bar{u}_j}{\partial x_i} \right)$. ν_{sgs} is the sub-grid scale viscosity. The term $\frac{1}{3} \tau_{kk} \delta_{ij}$ is accounted for through the introduction of a modified pressure (i.e. $\bar{P}^* = \bar{P} + \frac{1}{3} \tau_{kk} \delta_{ij}$).

In the energy equation, the term Π also needs to be modelled and is computed as:

$$\Pi_{\text{sgs},i} = \frac{\nu_{\text{sgs}}}{\text{Pr}_t} \frac{\partial \bar{T}}{\partial x_i} \quad (5)$$

where (Pr_t) is the turbulent Prandtl number. Equation 4 and 5 require the sub-grid viscosity (ν_{sgs}) and for the present simulations the Wall Adapting Local Eddy (WALE) viscosity model shown in Equation 6 by Nicoud and Ducros[17] is used:

$$\nu_{\text{sgs}} = (C_m \cdot \Delta)^2 \frac{\left(\overline{S_{ij}^d S_{ij}^d} \right)^{3/2}}{\left(\overline{S_{ij} S_{ij}} \right)^{5/2} + \left(\overline{S_{ij}^d S_{ij}^d} \right)^{5/4}} \quad (6)$$

where $\overline{S_{ij}^d}$ is defined as $\frac{1}{2} \left(\left(\frac{\partial \bar{u}_i}{\partial x_j} \right)^2 + \left(\frac{\partial \bar{u}_j}{\partial x_i} \right)^2 \right) - \frac{1}{3} \delta_{ij} \left(\frac{\partial \bar{u}_i}{\partial x_j} \right)^2$. Δ is the grid size, which is computed as $(\Delta x, \Delta y, \Delta z)^{1/3}$. C_m is a model constant and in Code_Saturne is taken to be 0.25.

180 Concerning the discretisation schemes employed, the temporal and spatial schemes are second order with the Crank-Nicholson and Second Order Linear Upwind (SOLU) schemes used, respectively.

2.2. Geometry

The heating rods are arranged into three concentric ranks, which are enclosed by a cylindrical
 185 containment (see Figure 1). Diameters for the rod and containment are 0.0153 m and 0.1923 m, respectively. The rods are split into the three aforementioned ranks, which are radially located at 0.025 m, 0.051 m and 0.079 m. A representative p/d ratio of 1.8 can be given for the whole bundle.

A block structured mesh consisting of ≈ 77 million elements is generated. Using data from the highest heating case and a physical distance (y) defined as that between the first cell centre
 190 and wall, the peak y^+ value in the domain is ≤ 0.52 , indicating the first mesh cell nodes are within the viscous sublayer. The values for the spanwise and streamwise grid spacing calculated at mid-height are $\Delta x^+ = 44.5$ and $\Delta z^+ = 35.7$, respectively. The mesh cross-section is given in Figure 1.

In transition regions, results from LES have been shown to have a grid dependency[6, 18].
 195 Looking at work from researchers such as Nakao et al.[18], and Barhaghi and Davidson[6] differences in grid sizing altered the point of transition (and statistics within this region). However, statistics in the laminar and turbulent regions were largely independent of the mesh size. Consequently, it is expected that the particular location of transition may vary somewhat, but flow development pre-transition and the turbulent flow characteristics after transition are reliable. Nonetheless,
 200 less, during grid generation, the earlier work of other researchers has been considered with the

vertical grid spacing at mid-height roughly corresponding to that reported by Nakao et al.[18].

2.3. Properties, boundary conditions and numerical setup

Carbon dioxide at a pressure of 3 MPa is the working fluid. Density is temperature dependent and is modelled using data obtained from the National Institute of Standards and Technology[19].

205 The remaining physical properties are specified as constants and their values are given in Table 1.

Table 1: Physical property constants imposed on the fluid

Property	Value	Units
Dynamic viscosity	2.712×10^{-5}	Pa s
Thermal conductivity	0.04	W/m°C
Specific heat	1088	J/kg°C
Prandtl number	0.737	-

As seen in Figure 1, the geometry is reduced to a 60° sector. Although reduced, there are still multiple sub-channels available in the sector, and as will be shown later, away from the domain ends and point of transition the flow is primarily constrained to the sub-channels. The azimuthal ends of the sector are modelled using rotational periodicity. The top, bottom, and central rod (guide tube) walls are adiabatic. A constant heat flux boundary condition is applied at the rod wall and the values used are given in Table 2. A convective boundary condition is assigned at the 210 containment surface with a fixed heat transfer coefficient of $700 \text{ W/m}^2\text{°C}$ and sink temperature of 110°C . Finally, all the surfaces concerning the flow are modelled as smooth walls.

Table 2: Case definition

Case name	Heat flux
Case-1	1154 W/m^2
Case-2	289 W/m^2

2.4. Non-dimensional parameters

215 The characteristic length of the rod bundle cavity can be defined in multiple ways. For example, one can take the characteristic length as the distance between the hot and cold surfaces, as typically done for simple cavities. Alternatively, the hydraulic diameter of the sub-channel can be used. This is to treat the flow through the interior sub-channels as analogous to a heated pipe flow (this is discussed later).

220 Natural circulation flow in cavities can be characterised by the Rayleigh number, aspect ratio and Prandtl number. As seen in Table 1, the Prandtl number is fixed to 0.74. The aspect ratio (A) is defined as H/L where H is the height and L is length scale of the flow passage. Taking the length scale to be the distance between the heating rod surfaces and the cooling containment wall, the aspect ratios are 14, 22 and 57 ordered from the first to last rank. Using the mean internal sub-
225 channel hydraulic diameter as the length scale gives an aspect ratio of 23. The Rayleigh numbers based on the heat flux and temperature definition are now computed using the bundle height (H), minimum and maximum length scales (i.e. $L1$ and $L3$ for Rank-1 and Rank-3, respectively). These values are given in Table 3.

Table 3: Rayleigh numbers for the heating cases considered using different length scales. $Ra_{\Delta T_V}$ is computed using the overall domain maximum and minimum temperatures.

Parameter	Case-1	Case-2
$Ra_{H,\Delta T_V}$	1.23×10^{13}	7.6×10^{12}
$Ra_{L1,\Delta T_V}$	4.5×10^9	2.7×10^9
$Ra_{L3,\Delta T_V}$	6.7×10^7	3.4×10^7
$Ra_{H,q''}$	1.5×10^{15}	7.97×10^{14}
$Ra_{L1,q''}$	3.4×10^{10}	2.1×10^{10}
$Ra_{L3,q''}$	1.4×10^8	7.5×10^7

The Rayleigh numbers are computed using the following definitions; $Ra_{\Delta T} = g\beta\Delta TL^3 / (v\alpha)$
230 and $Ra_{q''} = g\beta q'' L^4 / (v\alpha\lambda)$.

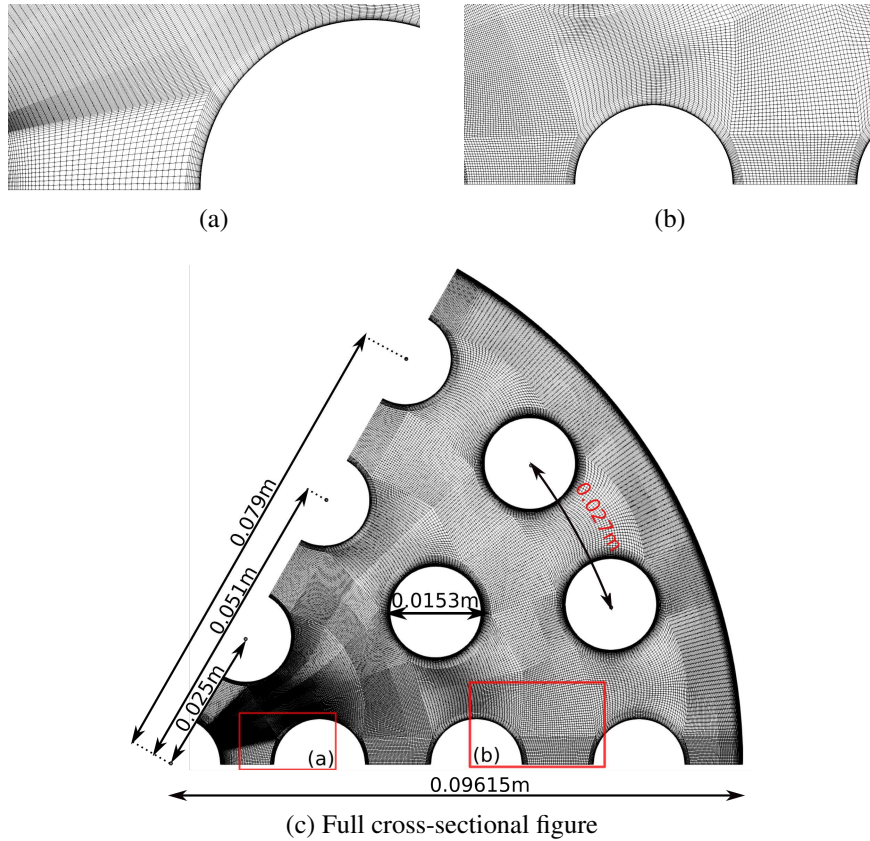


Figure 1: Cross-sectional resolution of the mesh used in the LES computations.

3. Results

A schematic of the data extraction locations and sub-channel divisions is given in Figure 2. The direction in which the profiles are plotted is given by the arrow direction, with $(y/y_{max} = 0)$ being the tail end.

235 In the simulations, a fixed time step of 0.0004 s is used for all the cases. This gives a peak Courant number of approximately 1. However, in a few isolated cells ($\ll 0.1\%$) for the highest heating case the Courant value fluctuates above 1. In the majority of the cells, the peak Courant values are well below 0.5 and the peak spatial mean is ≈ 0.1 at any given instance. A further reduction in the time step value to control the peak Courant value in the isolated cells would mean
 240 a large portion of the domain would have cells with essentially zero Courant numbers (bringing

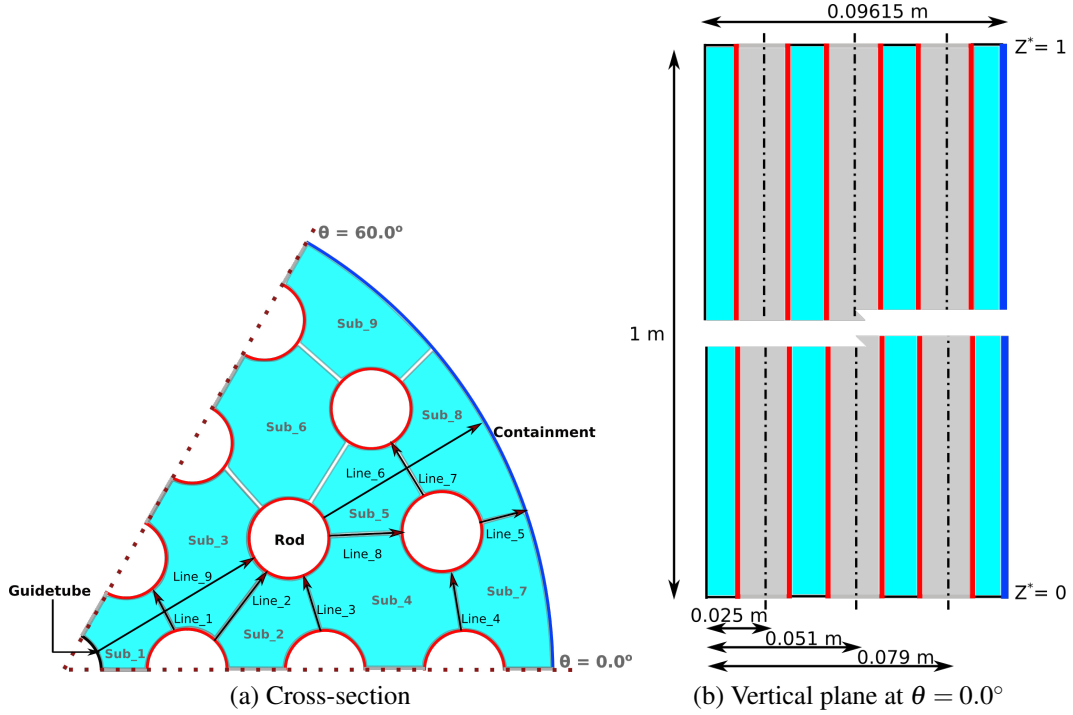


Figure 2: Schematic of the sub-channel divisions (denoted by Sub-*), the extraction locations for the profiles and a vertical plane. The adiabatic guide tube is coloured black. The fuel rods have a constant heat flux boundary condition and are coloured red. The cooling containment wall has a convective boundary condition and is coloured blue.

the spatial mean to well below 0.1).

Barring the numerical implications of the chosen time step, it also must be assessed in terms of the accurate resolution of the flow physics. To achieve the aforementioned, a viscous time step is computed for the containment surface here, the flow transitions from laminar to highly turbulent (will be discussed later). The viscous time step is thus defined as:

$$\Delta t = \frac{\nu}{w_{\tau}^2} \quad (7)$$

The computed wall time step based on the LES simulation data for case-1 and case-2 is shown in Figure A1 in the appendix. As can be seen, the lowest time step is approximately 7.5×10^{-4} , while the one used in the simulation is 4×10^{-4} . This demonstrates the time step used is conser-

245 vative in terms of flow physics, and such a small time step is due to the requirement of numerical stability.

Once the LES simulation converges, the averages are restarted, and the statistics calculated over a period slightly longer than 100 s for both cases. To assess the convergence of the statistics, profiles are extracted along Line_1 and Line_5 in Figure 3 (see Figure 2 for the data extraction location). The profiles are plotted at three-time points, and the comparison clearly shows a well-
 250 converged solution.

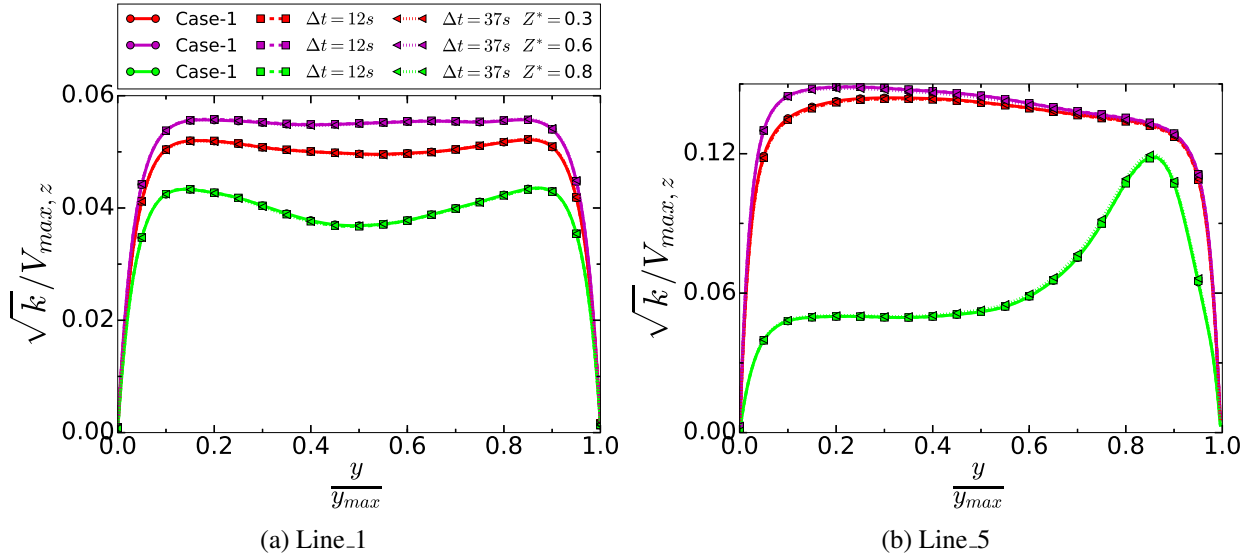


Figure 3: Turbulent kinetic energy plotted at different times for case-1 at Line_1 and Line_5 (Extraction locations are given in Figure 2). Please note the time difference in the plots is that from the final time point to the respective comparison time points.

LES_IQ_v can be used to determine the LES simulation quality, the parameter was proposed by Celik et al.[20] and is defined as shown in Equation 8.

$$\text{LES_IQ}_v = \frac{1}{1 + 0.05 \left(\frac{S^*}{1-S^*} \right)^{0.53}} \quad (8)$$

S^* is computed as shown in Equation 9. Where it has been taken sub-grid viscosity is equal to the

255 numerical viscosity i.e. $\mu_{\text{sgs}} \approx \mu_{\text{num-diff}}$.

$$S^* = \frac{\mu_{\text{sgs}} + \mu_{\text{num-diff}}}{\mu_{\text{sgs}} + \mu_{\text{num-diff}} + \mu} \quad (9)$$

Computations are considered to be good if this value is above 0.8. Computing this parameter gives a minimum value (considering both cases) of 0.91. Contour plots of this parameter are given in Figure A2.

3.1. Global - flow pattern

260 The general behaviour of the flow, turbulence, and thermal fields is illustrated on a vertical plane at $\theta = 30^\circ$ in Figure 4. From left to right, the walls are those for the insulated guidetube, side walls (left and right) of a heated second rank rod, and the cooled containment wall. Consequently, the “channel” on the left is typical of an asymmetrically heated channel, whereas that on the right is typical of a heating and cooling channel. For figure 4, the velocity and turbulent
265 kinetic energy contours are normalised using the buoyant velocity ($V_{n,\Delta T_V}$), which is defined as $V_{n,\Delta T_V} = (g\beta\Delta T_V\nu)^{1/3}$. The temperature difference (ΔT_V) used for the buoyant velocity is that between the domain maximum (T_h) and minimum (T_c). Similarly, the temperature contour plot is normalised using the maximum and minimum difference. Contour plots illustrating the cross-sectional behaviour are extracted at several axial locations and shown in Figures 5 and 6, for the
270 velocity and turbulent kinetic energy, respectively. To show the local variation at each axial location, the cross-sectional contours are normalised using the absolute peak velocity of the slice.

Considering figures 4, 5 and 6 in conjunction, the flow can be split into three definitive vertical regions, which are initially briefly introduced in listed form below.

The Z^* locations and the ensuing discussions below are representative for both case-1 and
275 case-2:

- The top region at $Z^* \approx 0.75 - 1.0$: This region is largely made of a stagnant stratified fluid with a thin downward laminar boundary layer on the cooling containment wall and turbulent upward boundary layers on the heated rods.
- The middle (main section) region at $Z^* \approx 0.15 - 0.75$: In this region, the flow is highly turbulent with a large scale downward flow near the containment and an upward interior flow in the sub-channels formed between the fuel rods/guidetube.
- The bottom region at $Z^* \approx 0.0 - 0.15$: This region is characterised by the downward flow impingement and a cross-flow.

3.1.1. The top region

Figure 4(a) particularly highlights the developing boundary layer flow at the containment surface, boundary layer flow at the rods and a largely stagnant region away from the walls. Little or no turbulence levels are observed at the containment surface. However, transition to turbulence occurs towards the lower part of this region and when this occurs, turbulence is initially generated where the gap is narrowest with the third rank rods (Figure 6(e)). These peaks form close to the containment surface and are a result of the shear production of turbulence. The onset of transition in enclosures is known to be aspect ratio dependant and this seemingly leads to initial turbulence generation occurring where the distance between the hot and cold surfaces is at a minimum and thus aspect ratio is largest.

Figure 4(a) also shows the flow on the rods is constrained to the boundary layers, which reduce in thickness as the flow ascends. Eventually, close to the top wall, the boundary layer flow stagnates due to the end effects and stratification. Turbulence is shown to occur in the regions surrounding the rods with little or no turbulence at the cores, which also happen to be regions of stagnant flow. One of the characteristics of boundary layer flow regimes in cavities is vertical

temperature stratification. As seen in Figure 4(c), the vertical temperature distribution is heavily
300 stratified for the top region. The cross-sectional temperature distribution (not shown) is uniform
with significant temperature gradients only occurring across the boundary layers.

Due to the effects of buoyancy, the flow ascends at the heated rod surfaces and descends at
the cooled containment wall with a general clockwise rotation thereby forming the primary flow
circulation. Figure 5(f) shows close to the top wall as part of this circulation, the hot gas traverses
305 from the interior sub-channels to the containment wall with relatively high cross-flow magnitudes.

3.1.2. Middle region

The middle region makes up most of the cavity and is dominated by turbulence effects. Tran-
sition to turbulence at the containment surface is qualitatively shown to occur at a dimensionless
distance (Z^*) of approximately 0.8, with the turbulent region commencing at $Z^* \approx 0.75$. This is
310 particularly illustrated in Figures 4(a & b) by the sudden expansion of the boundary layer thickness
and the drastic increase in turbulence levels at this location.

At the point of transition, the flow is entrained from the interior towards the containment wall
due to the rapid growth of the boundary layer thickness. Figure 5(d) shows the cross-flow vector
magnitudes are significantly greater than those observed close to the top wall. Enhanced chaotic
315 mixing occurs from here on and is perhaps best characterised by the ensuing nearly uniform verti-
cal fluid temperature. This is in stark contrast to the top region, which is heavily stratified.

When transition occurs, the turbulence peaks are initially located close to the containment
surface. However, with depth a large scale downward flow structure exists on the right-hand side
where cooling occurs. This flow structure is strong and extends well beyond the containment
320 wall. Figure 5(c) shows the flow is entirely downward up to the third rank rod gap, essentially
there is heated downward flow or buoyancy opposed flow at this surface. On the left-hand side,

the interior channel flow is entirely upwards. The vertical vector plots in Figure 4(a) indicate an acceleration of the interior channel flow from the bottommost to approximately the mid-height $Z^* = 0.5$. This is seemingly followed by a deceleration region, culminating to much-reduced flow
325 vector magnitudes at the top of the middle region.

These two opposing flows interact at the gaps of the third rank rods and the black contour line for $\bar{w}/V_{max,z} = 0$ demarcates them. Below $Z^* = 0.75$, turbulence peaks are located near here indicating this shear layer dominates turbulence production. Turbulence spreads from here to the interior sub-channels and this is best illustrated by Figure 6(c). At the interior rod gaps, high free-
330 stream turbulence levels are evident and from a qualitative viewpoint appear to prevail over the local turbulence production at the rod surfaces.

Earlier on, two channels separated by the second rank rod were identified (see Figure 4). On the right-hand side (heating and cooling) channel, the flow strongly resembles that of the Betts and Bokhari case study [4], and for the left-hand side channel, the behaviour is that of a heated
335 upward flow. Third rank rods encapsulated within the right-hand side channel appear to act as mere obstructions to the flow and generation of turbulence (see Figures 5(c) and 6(c)). It is quite interesting to note, at the third rank rod walls facing the containment surface, there is no evidence of upward flow in the turbulent region. On this portion of the rod wall, the local mean flow opposes the buoyancy force (buoyancy opposed flow) and the lack of upward flow near here gives a further
340 indication of the strength of the downward flow.

Keyhani et al.[15] conducted experiments in a 3 x 3 and 5 x 5 rod bundle. The reported flow visualisation results in their paper were based on the 3 x 3 rod bundle at a Rayleigh number (based on the containment diameter) of 2.97×10^7 . The Prandtl number was 46 as ethylene glycol with suspended aluminium particles was used to aid flow visualisation. The flow descriptions in
345 their study closely resembled those of the top region in the present simulations. Boundary layer

flow was observed and the rods did not interact with each other. In cavities, the flow regime is dependant on the Rayleigh number, Prandtl number and aspect ratio. A higher aspect ratio decreases the critical Rayleigh number required for the onset of transition, while a higher Prandtl number increases the critical Rayleigh number. The aspect ratio for their study based on the 3 x 3 hydraulic diameter is ≈ 13 , compared to 23 for the current study. In the visualisation study by Keyhani et al.[15], the Prandtl number was higher 46 compared to 0.737 in the present simulations. Finally, the Rayleigh number (based on the containment diameter) in the current study is $\approx 2.5 \times 10^9$, which is larger than those considered in their flow visualisation experiments. The difference in flow visualisation reflects the differences in the flow regimes that exist in the two studies: largely laminar in Keyhani et al.[15] whereas mostly turbulent herein.

3.1.3. Bottom region

The bottom region starts below $Z^* = 0.2$, where the boundary layer at the containment wall begins to show a decrease in thickness. Within this region, the flow is diverted towards the interior from the containment and it is shown, the cross-flow vector magnitudes increase approaching the bottom wall (see Figure 5(a & b)). In Figure 6, the overall local peak turbulence values occur at $Z^* = 0.01$ and close to the containment wall. At this location, the downward flow impinges onto the bottom wall increasing turbulence production.

In the interior, the flow begins its ascent from the bottom of the rods. It is readily apparent the boundary layer at the rods has a shorter development length in comparison to that observed at the containment wall. However, as seen in Figure 4 there is a difference in the rod flow development based on the two channels identified earlier. On the left-hand side channel, the heated rod wall is on the leeward side of the cross-flow. Away from the rod wall (going further left to the adiabatic wall) there is stagnant to very low magnitude downward flow. Initially, a boundary layer is observed

on this surface. In contrast, on the right-hand side, where the rod is directly facing the cross-flow
 370 no stagnant region is observed. Instead the upward and descending flows still interact even quite
 close to the bottom wall. Visually, the development of the boundary layer on the rod here appears
 somewhat affected by the impinging cross-flow and stronger convected turbulence.

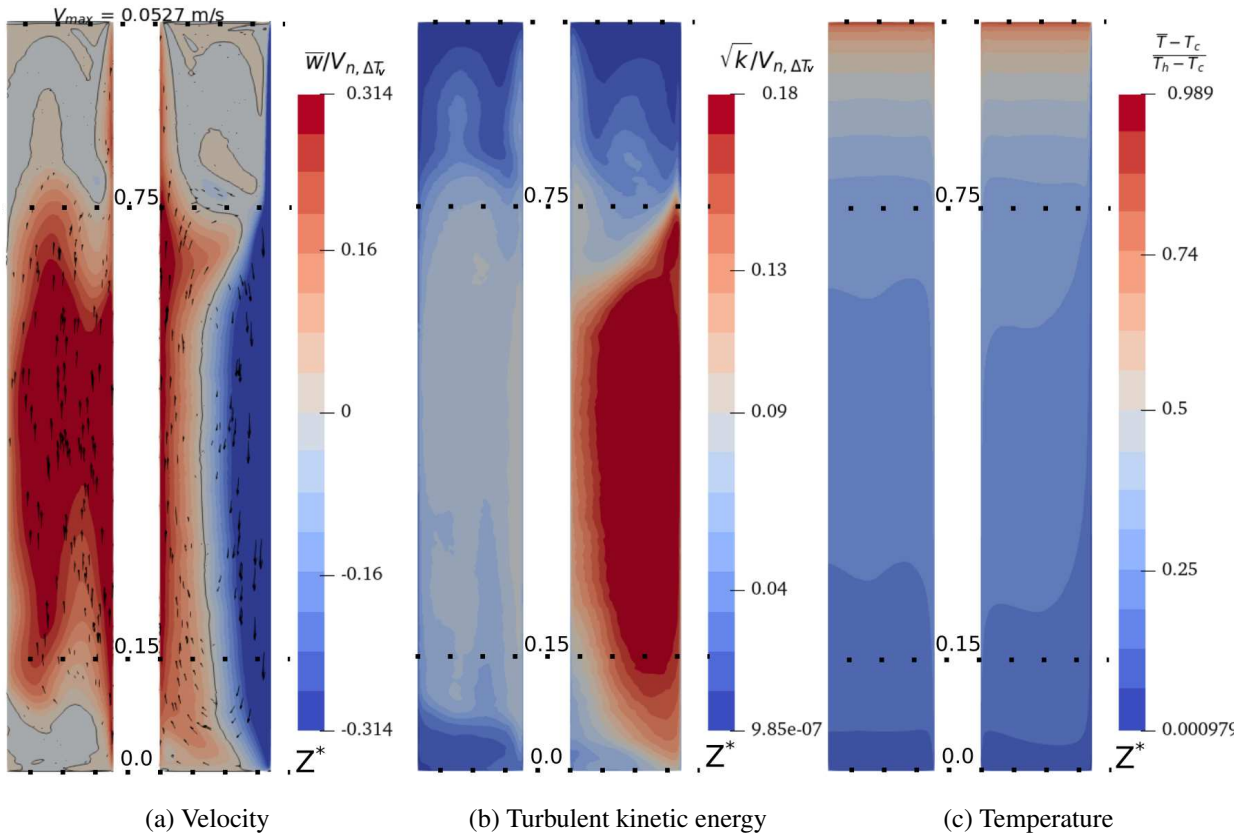


Figure 4: Contours of turbulent kinetic energy, velocity and temperature extracted from Case-1. Slices are taken at $\theta = 30^\circ$. The black contour line (only shown for velocity) is specified at $\bar{w}/V_{\max,z} = 0.0$. To better represent the data, the height of the domain is shrunk by a factor of 4.

3.2. Statistical distributions

Global contour plots have shown the overall flow behaviour in the bundle differs not just ver-
 375 tically but also based on the sub-channel. The channels are split by the second rank rod as seen
 in Figure 4. The discussion of the profiles is therefore further split into two regions based on the

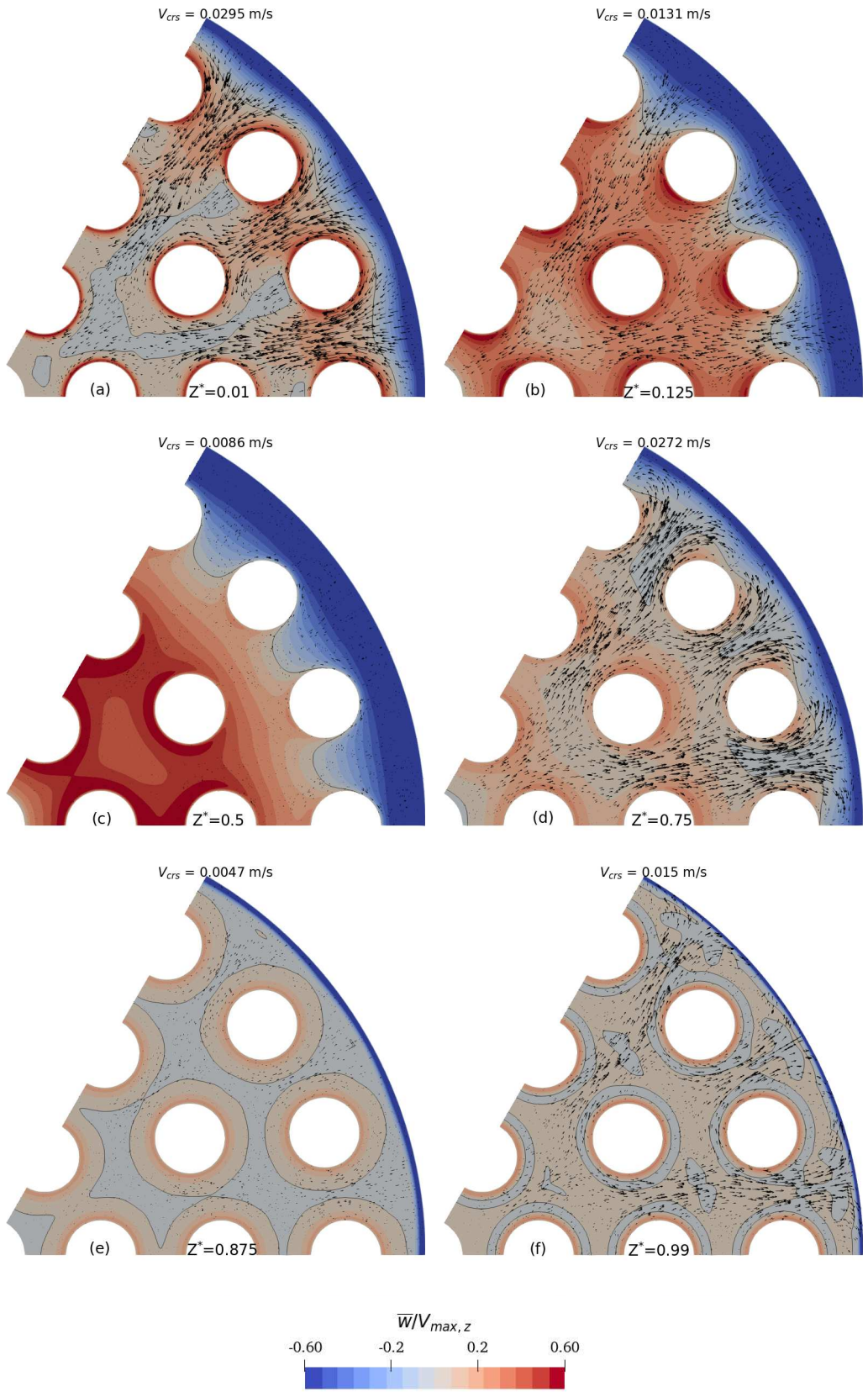


Figure 5: Axial velocity contours extracted for Case-1. Contours at $\bar{w}/V_{\max,z} = 0.0$ are marked with a black line. $V_{\max,z}$ is used in normalisation and is the peak axial velocity of the slice. A dimensional value for the cross-flow peak (V_{crs}) is given.

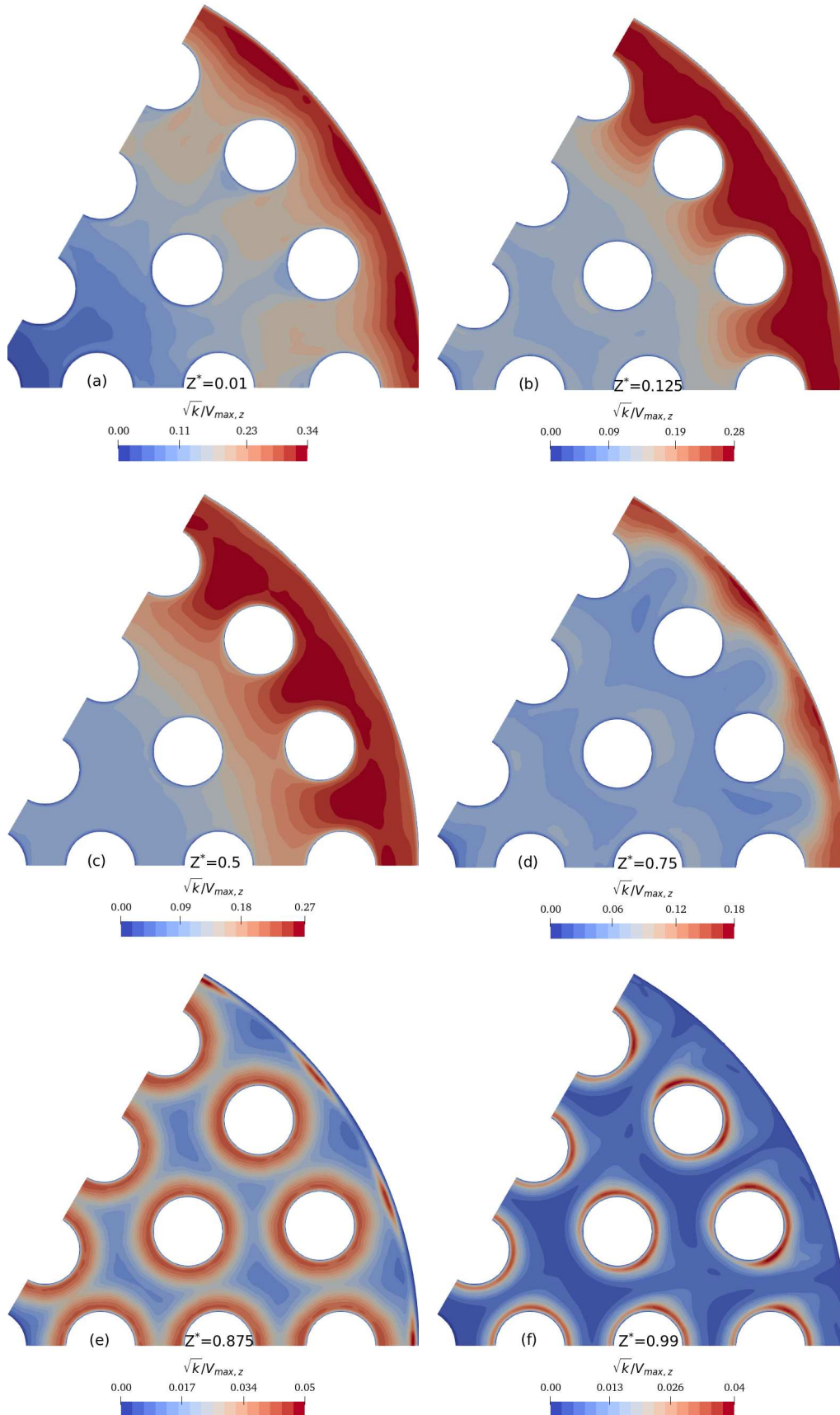


Figure 6: Contour plots turbulent kinetic energy extracted for Case-1. The contours are normalised using the peak velocity of the slice and a scalebar is shown for each subfigure to maximise the variation.

defined channels which are; the heating and cooling outer channel, likened to Betts and Bokhari case study[4] including sub-channels 4 to 9 and the heated upflow central channel, including sub-channels 1 to 3.

380 3.2.1. Outer region

Velocity, temperature, and turbulent kinetic energy profiles are shown in Figures 7 to 9. The profiles are extracted from Line_5 and Line_6, representing the narrow and large gaps existing in this region respectively, with the locations of these lines illustrated in Figure 2. First we note that the profiles for cases 1 and 2 are very close to each other and in the following discussion, we will
385 not distinguish between them unless stated otherwise. The velocity profiles are normalised using the buoyant velocity. The vertical temperature difference (domain maximum (T_h) and minimum (T_c)) is again used to fix the buoyant velocity and show the development of the velocity profiles. For the turbulent kinetic energy profiles given in Figure 9, the normalisation is carried out using the peak streamwise velocity at the extraction location. Using the peak streamwise velocity allows
390 for the comparison of turbulence levels to general flows. Temperature profiles are given in Figure 8. These profiles are computed using the local maximum $T_{h,z}$ and minimum $T_{c,z}$ temperatures.

Line_6 is extracted from the second rank rod to the containment surface. This line exhibits the typical behaviour expected of an opposing upward and downward flow in a heating and cooling channel. In the top region, the boundary layer is thin (and of laminar nature as will be further
395 shown later) at $Z^* = 0.8$ and $Z^* = 0.9$. This is supported by the turbulence kinetic energy profiles, which show little to no turbulence levels here. In the next section, a similarity comparison is carried out for the laminar containment flow. At $Z^* = 0.7$, the flow is clearly turbulent but still developing and it becomes fully developed between $Z^* = 0.6$ to $Z^* = 0.3$, as seen from the identical profiles for turbulence and velocity. Below $Z^* = 0.2$, the flow profiles start to alter due to the encroaching

400 end effects.

The temperature profiles are also similar to each other between $Z^* = 0.6$ to $Z^* = 0.3$. Temperature variation is quite significant near the walls, however away from the walls a uniform temperature core is seen and this remains true from the top wall right-down to the bottom wall. In contrast for velocity, the core is initially stagnant at the top region ($Z^* = 0.9$ and $Z^* = 0.8$). In the
405 middle highly turbulent region, the boundary layers between the opposing flows strongly interact with each other resulting in a linear gradient profile across the gap. Turbulence peaks as observed in the contour plots occur in the core as a result of the second shear layer. The aforementioned flow behaviour is similar to the observations made by Betts and Bokhari[4].

Line_5 is extracted from the third rank rod to the containment wall. At the top region, the flow
410 is constrained to the boundary layers, with a stagnant core similar to that along Line_6 even though with a thinner boundary layer. But in contrast to that along Line_6, in the turbulent region the entire flow is going downwards, clearly dominated by the strong cooling effect on the containment wall. This region of buoyancy opposed flow on the rod extends from $Z^* = 0.7$ to $Z^* = 0.2$. This is the only location in the domain where such a scenario arises. At all the other heated or cooled surfaces
415 buoyancy aided flow is prevalent. It should be noted however that the buoyancy does cause the velocity gradient to be lower on the rod than on the opposite wall as expected. Turbulence peaks across this gap are shown to be broad and flat in comparison to those for Line_6, which have a peak in the interior.

3.2.2. *Central region*

420 Velocity, temperature, and turbulent kinetic energy profiles for this region are given in Figures 10 to 12. Normalisation of the profiles is as discussed in subsection 3.2.1. The flow in the left-hand side region is primarily heated upflow but with interference from the right-hand side region.

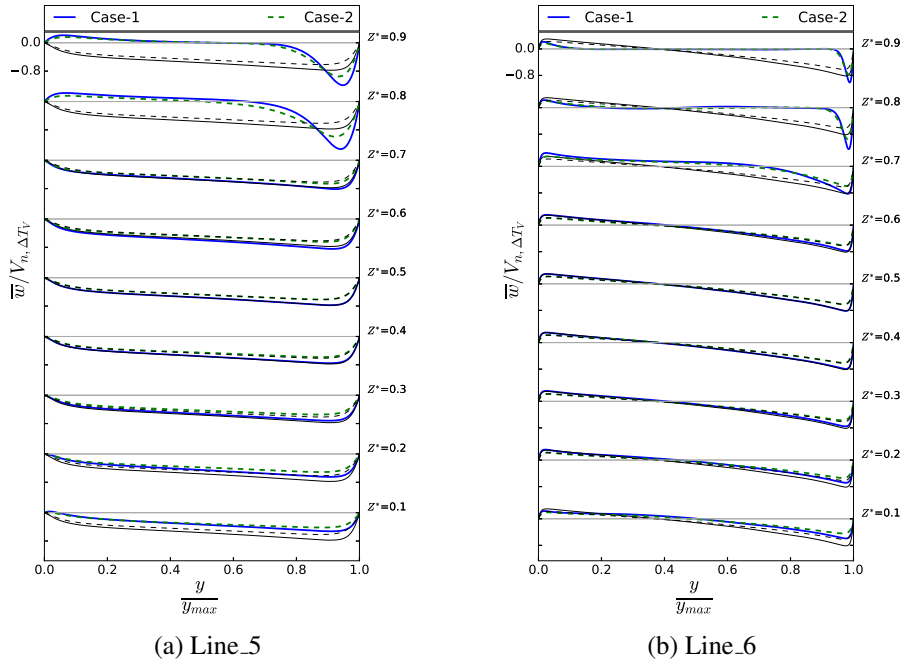


Figure 7: Outer region profiles for the axial velocity at different heights. The profiles are normalised using the buoyant velocity ($V_{n,\Delta T_V} = (g\beta\Delta T_V\nu)^{1/3}$). The profile at mid-height ($Z^* = 0.5$) is added to each subplot using black-thin lines.

The profiles shown are obtained from Line_1, Line_2, and Line_9. Line_1 and Line_2 are extracted across the rod gaps, while Line_9 can be considered an extension of Line_6 to the left-hand side
 425 region and spans from the heated second rank rod to the adiabatic guide tube wall.

At the rod gaps (Line_1 and Line_2) as the flow ascends, the boundary layers on the opposing rod surfaces merge. Between $Z^* = 0.1$ and 0.7 , the free-stream turbulence levels at the gap centres are quite significant. This is due to turbulence spreading from the right-hand side, thus we see a departure from the typical natural convective flow profile to one more typical for forced/mixed
 430 convection flows between $Z^* = 0.2$ to $Z^* \approx 0.6 - 0.7$. Above these heights in the top region, free-stream turbulence levels began to drop at the rod gaps as there is less turbulence convected from the right-hand side. The flow is now constrained to the boundary layers. The increasing end effects and stratification eventually destroys the vertical boundary layer flow. The profile for Line_2 is asymmetric at $Z^* = 0.1, 0.7,$ and 0.8 . This occurs as the profile straddles the first and

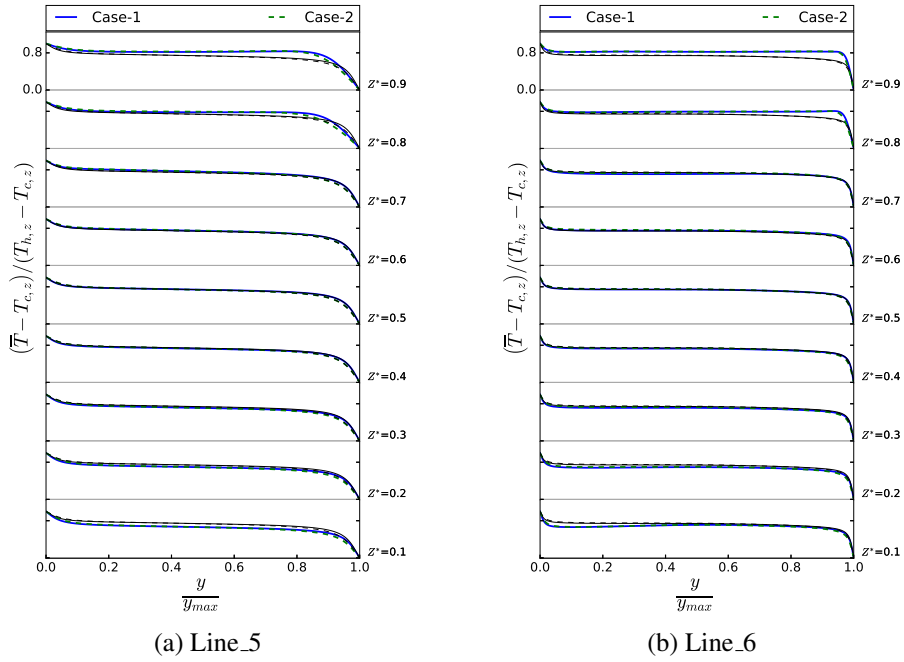


Figure 8: Outer region temperature profiles extracted at differing axial locations. The profile at mid-height ($Z^* = 0.5$) is added to each subplot using black-thin lines.

435 second rank rods, thus is heavily influenced by the cross-flow at these locations.

The temperature profiles for Line_1 and Line_2 show the boundary layer thickness is largely unchanged with height and hence showing the profile typical of a fully developed internal channel/pipe flow. Changes in the thickness can however be seen at the transition from laminar to turbulence. Similar to the profiles shown for the right-hand side region, there is a largely uniform
 440 temperature core with significant temperature variation occurring across the boundary layers.

It is interesting to note for both Line_1 and Line_2, the peak amplitude of the velocity profile alters with height between $Z^* = 0.2$ and 0.7 . In particular, for Line_1, it can be noted below the mid-height flow acceleration occurs. Above mid-height between $Z^* = 0.6$ and 0.7 , the flow decelerates although the shape of the profile largely remains the same. Past $Z^* = 0.7$, the flow
 445 continues to decelerate though this is now coupled with a change in the profile shape. The flow does not appear to fully develop between $Z^* = 0.2$ and 0.7 . Across this gap, the flow is akin

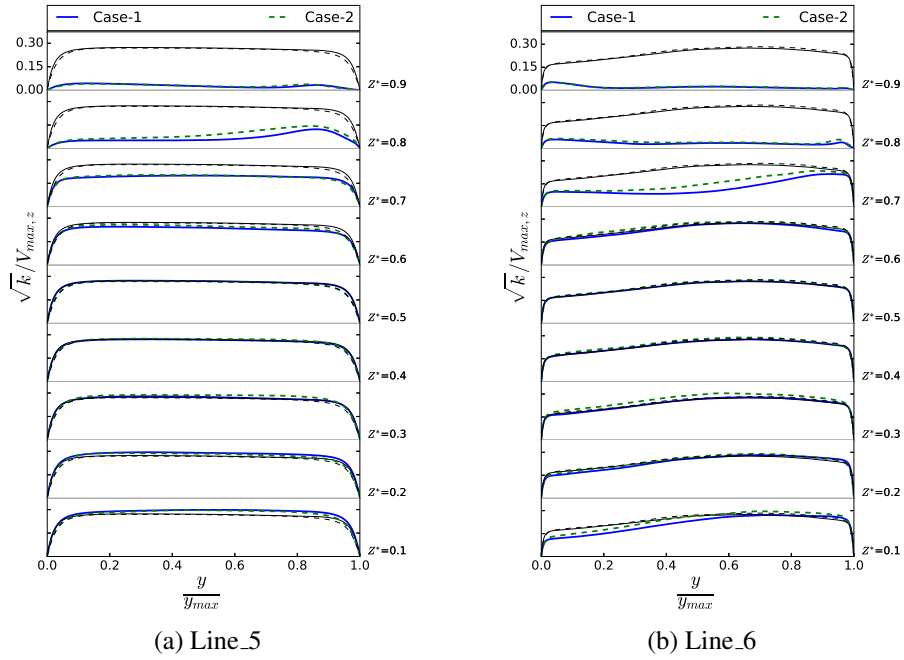


Figure 9: Outer region turbulent kinetic energy profiles extracted at differing axial locations. The local peak velocity of the profile is used in normalisation. The profile at mid-height ($Z^* = 0.5$) is added to each subplot using black-thin lines.

to that in a heated channel but due to its open boundaries, the chimney effect may draw flows from neighbouring such-channels causing the flow to accelerate. For example, results of Ohk and Chung[12] show due to the chimney effect flow acceleration occurred in their case study. A similar effect occurs here until $Z^* = 0.5$. Past the mid-height, cross-flow from the interior (left-hand side region) towards the containment (right-hand side region) gradually increases starting the deceleration process. Later on, inner scaling laws are used to check the self-similarity of the profiles in the turbulent region and bulk quantities at a sub-channel level are used to assess the influence of the cross-flow and bulk behaviour of the flow.

Line_9 generally follows similar trends to those discussed for the rod gap profiles, although there are a few dissimilarities. At the top region ($Z^* = 0.9$ and $Z^* = 0.8$) there is heated boundary layer flow on the rod surface. Away from this surface, the flow is stagnant up to the adiabatic guide

460 tube wall. In the middle region, there is an upward flow throughout the entirety of the profile. The influence of the strong downward flow structure in the outer region and the spread of turbulence as seen in Figure 10 and 12 propagates all the way to the guide tube wall. Away from the top/bottom developing regions, the flow is akin to a forced convection on the insulated guide tube side. Close to the heated rod however, the velocity profile shows a characteristics of one in a strongly heated upward pipe flow, which normally show a M-shape profile.

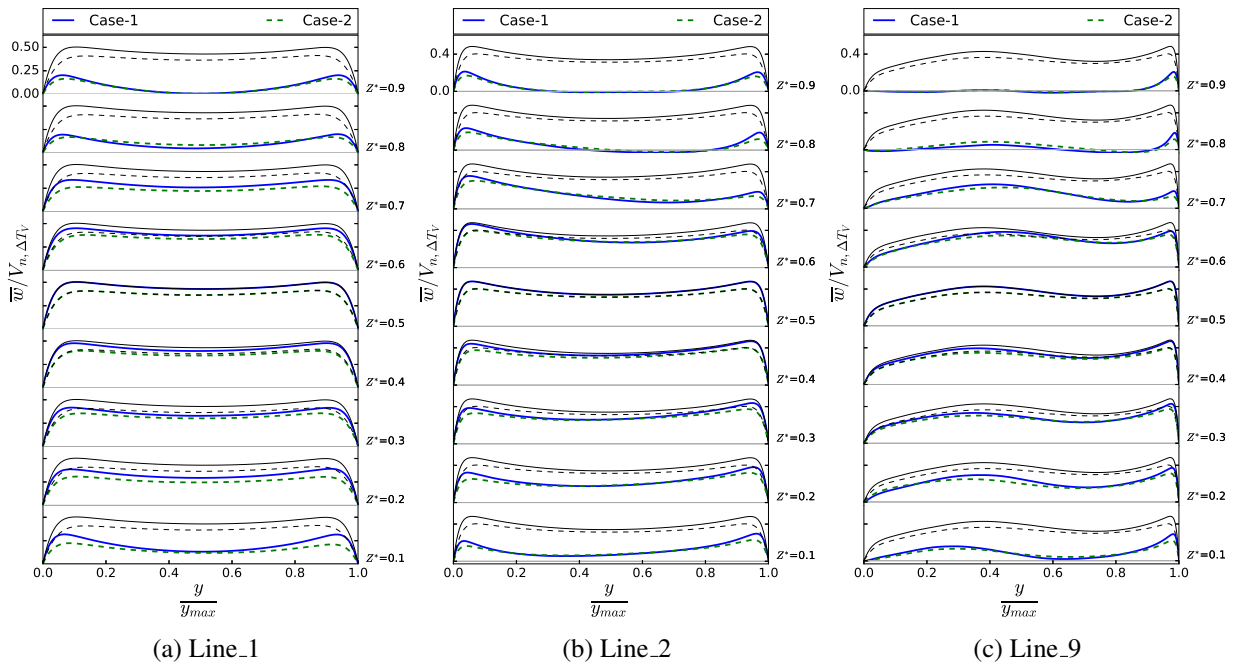


Figure 10: Central region profiles for the axial velocity at different heights. The profiles are normalised using the buoyant velocity $(V_{n,\Delta T_V} = (g\beta\Delta T_V\nu)^{1/3})$. The profile at mid-height ($Z^* = 0.5$) is added to each subplot using black-thin lines.

3.3. Laminar boundary layer

465 The initial flow at the top of the containment wall is laminar before transitioning to turbulence. Similarly, at the rods the flow would develop from an initially laminar state as it begins its ascent from the floor. In this section, comparisons are made against similarity solutions for buoyancy induced flows. Two similarity solutions are considered; at the containment surface the comparison

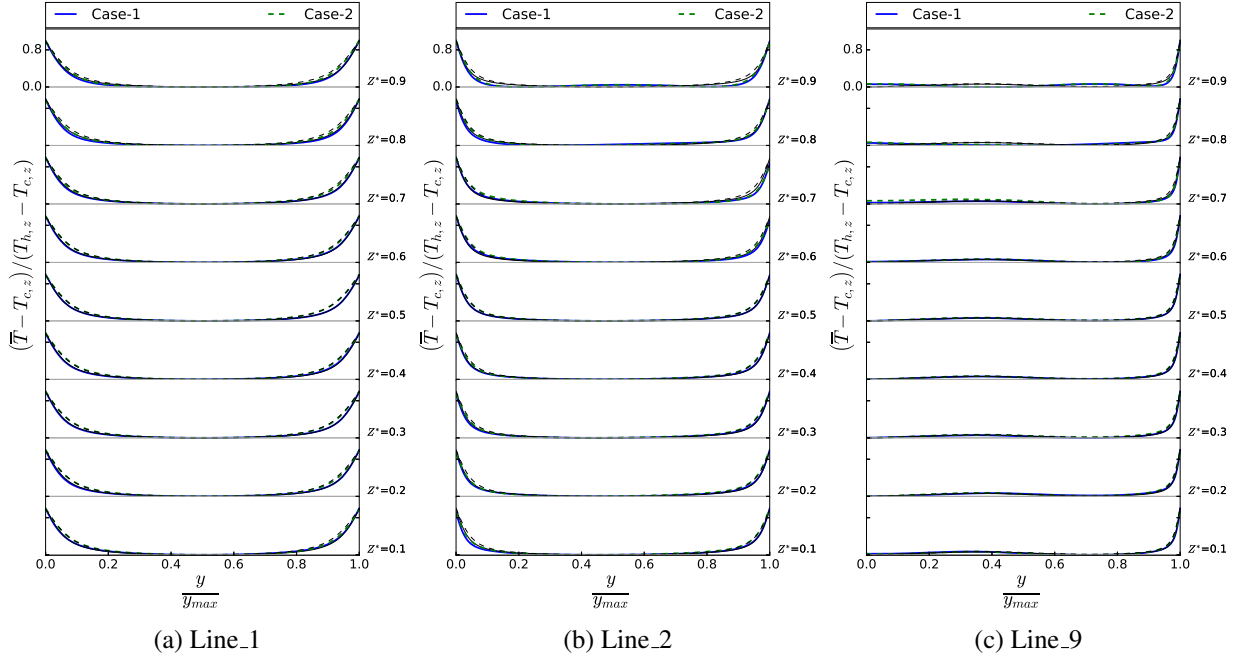


Figure 11: Central region temperature profiles extracted at differing axial locations. The profile at mid-height ($Z^* = 0.5$) is added to each subplot using black-thin lines.

is made against the similarity solution for buoyant flow on flat vertical surface by Ostrach[21]. At
 470 the rod surfaces, the comparison is against the slender cylinder similarity solution republished by
 Popiel[22] but originally from Sparrow and Gregg[23].

3.3.1. Similarity solution - Containment

In Ostrach's[21] similarity analysis, the stream function and similarity variable are defined as
 shown in Equation 10 to transform the momentum and energy into the form shown in Equation

475 11:

$$\eta = \frac{y}{z} \left(\frac{\text{Gr}_{z,\Delta T_H}}{4} \right)^{1/4} \quad (10a)$$

$$\Psi = F(\eta) \left[4\nu \left(\frac{\text{Gr}_{z,\Delta T_H}}{4} \right)^{1/4} \right] \quad (10b)$$

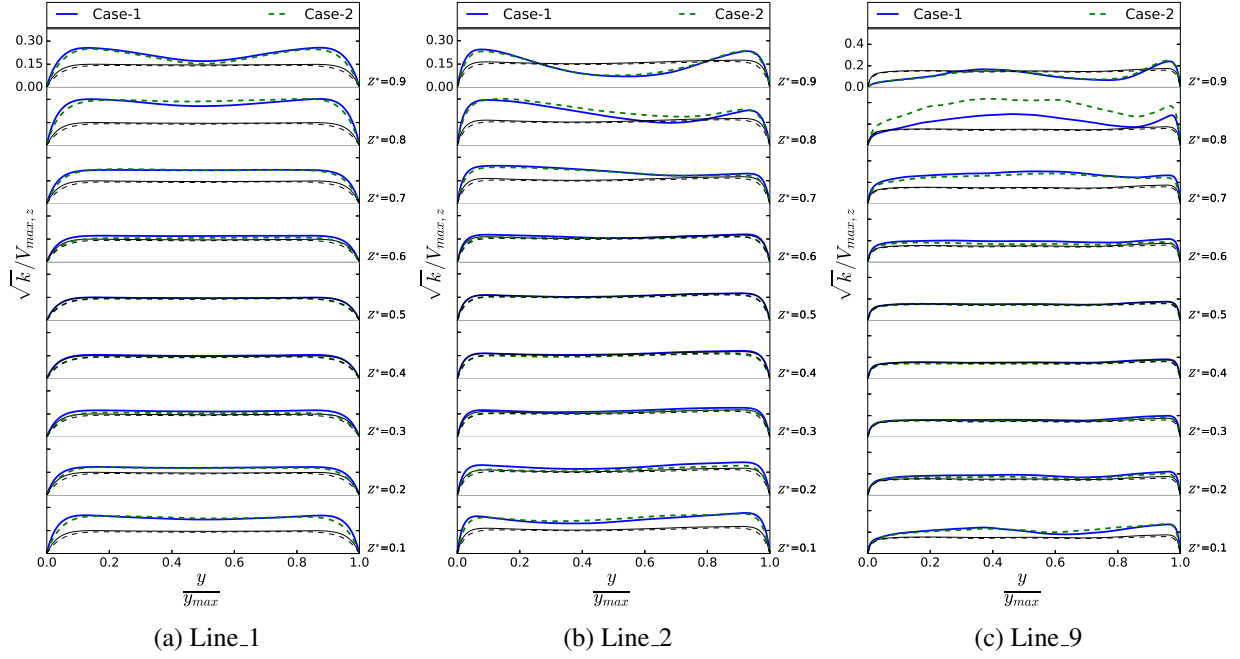


Figure 12: Central region turbulent kinetic energy profiles extracted at differing axial locations. The local peak velocity of the profile is used in normalisation. The profile at mid-height ($Z^* = 0.5$) is added to each subplot using black-thin lines.

$$F''' + 3FF'' - 2F'^2 + T^* = 0 \quad (11a)$$

$$T^{*''} + 3PrFT^{*'} = 0 \quad (11b)$$

where T^* is computed as $T - T_\infty / T_w - T_\infty$. The transformed equations for momentum and energy are higher order differentials and coupled together. Boundary conditions at $\eta = 0$ are given as; $F'(0) = F(0) = 0$, $T^*(0) = 1$ and those at $\eta = \infty$ are given as; $F'(\infty) = T^*(\infty) = 0$.

To compute the solution, initial values at $\eta = 0$ for $F''(0)$, which is the velocity gradient at the wall and $T^{*'}(0)$, which is the wall temperature gradient need to be obtained. This is done by firstly reducing the higher order differential equations (Equation 11) into a system of first order differential equations, this process yields five first order differential equations with three coming

from momentum and two from the energy equation. This system is solved using the explicit Runge-Kutta method. Since this is an initial value problem, the values for $F''(0)$ and $T^{*'}(0)$ which satisfy the given boundary conditions at $\eta = \infty$ need to be obtained. This is done by supplying the initial guess values and then iteratively solving until the successively updated approximate initial guess values satisfy the boundary conditions at $\eta = \infty$. To quickly check, if the solver is implemented correctly one can compare the predicted values against those from Ostrach's solution. At $Pr = 1$, Ostrach's values are 0.642 and -0.5667 for F'' and T^{*}' , respectively[21]. Setting $Pr = 1$, solutions from the implemented solver return similar values (identical to the third decimal place). The computed initial values are then used as boundary conditions and the system is again solved.

Similarity solution for velocity and temperature are shown in Figure 13 and 14 at the containment surface using Line_5 and Line_6 to compare with the LES simulation. The agreement is good for $Z^* > 0.83$ for Line_5 and $Z^* \geq 0.79$ for Line_6. Comparisons of the similarity solution against temperature show fairly reasonable agreement. Similar to velocity it is noted that Line_5 starts showing significant deviations at a shorter development length compared to Line_6. The difference in the location of the transition for Line_5 and Line_6 is likely due to the lengths of the lines, that is the gap sizes of the 'channels'. This is known to influence the the location of the transition. At Line_5, the rod is in much closer proximity to the containment wall and as seen from the turbulent kinetic energy contour plots at $Z^* = 0.75$ and 0.875 shown in Figure 6, there are turbulence peaks here in comparison to the rest of the containment wall. These contours show elevated turbulence regions on the containment wall locations adjacent to the third-rank rod.

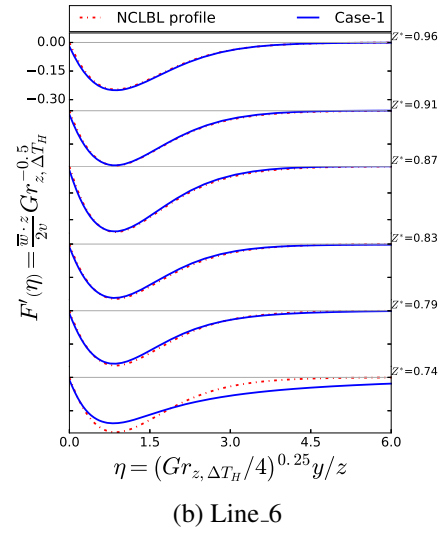
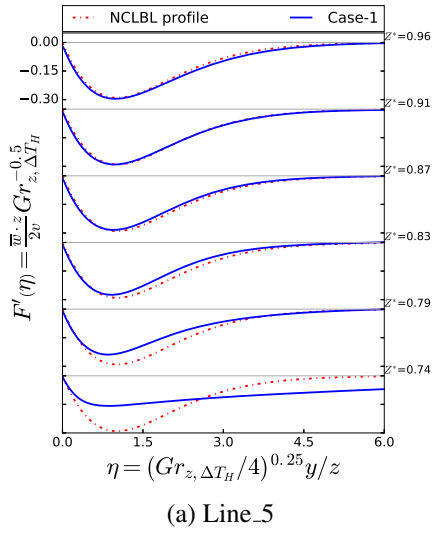


Figure 13: Velocity comparison of LES simulation data against the similarity solution by Ostrach[21] for Line_5 and Line_6. The containment surface is now located at $y/y_{max} = 0$. The top region from $Z^* = 0.96$ to $Z^* = 0.74$ is extracted

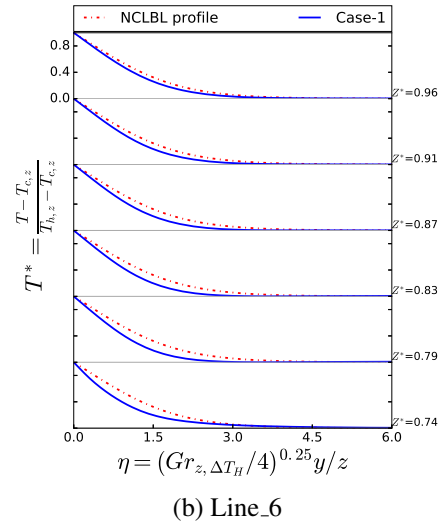
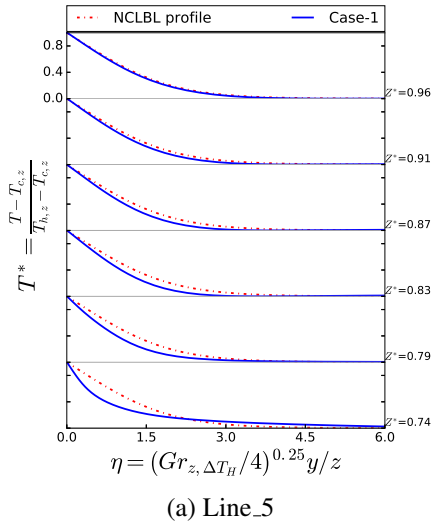


Figure 14: Temperature comparison of LES simulation data against the similarity solution by Ostrach[21] for Line_5 and Line_6. The containment surface is now located at $y/y_{max} = 0$. The top region from $Z^* = 0.96$ to $Z^* = 0.74$ is extracted.

3.3.2. Similarity solution - Rods

The similarity variable (η), radius of curvature effect (ξ) and the stream function (Ψ) are written as follows for the case of a slender cylinder[22]:

$$\eta = \text{Gr}_{R,\Delta T_H}^{1/4} \frac{R^{-7/4}}{2^{3/2}} \frac{(r^2 - R^2)}{z^{1/4}} \quad (12a)$$

$$\xi = \text{Gr}_{R,\Delta T_H}^{-1/4} \frac{2^{3/2}}{R^{1/4}} z^{1/4} \quad (12b)$$

$$F(\eta, \xi) = \text{Gr}_{R,\Delta T_H}^{-3/4} \frac{2^{3/2}}{\nu R^{3/4}} \frac{\Psi}{z^{1/4}} \quad (12c)$$

where R is the rod radius and z is the axial coordinate. The governing equations for momentum and energy are then transformed into[22]:

$$\xi \left(\frac{\partial F}{\partial \eta} \frac{\partial^2 F}{\partial \xi \partial \eta} - \frac{\partial F}{\partial \xi} \frac{\partial^2 F}{\partial \eta^2} \right) - F \frac{\partial^2 F}{\partial \eta^2} = \xi^2 \frac{\partial}{\partial \eta} \left[(1 + \eta \xi) \frac{\partial^2 F}{\partial \eta^2} \right] + \xi^4 T^* \quad (13a)$$

$$\xi \left(\frac{\partial T^*}{\partial \xi} \frac{\partial F}{\partial \eta} - \frac{\partial T^*}{\partial \eta} \frac{\partial F}{\partial \xi} \right) - F \frac{\partial T^*}{\partial \eta} = \frac{\xi^2}{\text{Pr}} \frac{\partial}{\partial \eta} \left[(1 + \eta \xi) \frac{\partial T^*}{\partial \eta} \right] \quad (13b)$$

In comparison to the similarity solution for a flat plate, the variables are now also a function of the radius of curvature ($F(\eta, \xi)$ and $T^*(\eta, \xi)$). These variables are equivalent to the series expansions shown in Equation 14. The first term in the series expansion is essentially the flat plate solution by Ostrach[21].

$$F(\eta, \xi) = \xi^2 [F_0(\eta) + \xi F_1(\eta) + \xi^2 F_2(\eta) + \dots] \quad (14a)$$

$$T^*(\eta, \xi) = T_0^*(\eta) + \xi T_1^*(\eta) + \xi^2 T_2^*(\eta) + \dots \quad (14b)$$

As shown by Popiel[22] and more in-depth by Goodrich[24], the series expansion can be substituted into the momentum and energy equation, yielding a set of coupled differential equations,

with the higher order series expansion terms dependant on the lower order terms. Herein, the series expansion is considered up to the second order term. The resulting system of equations are solved in a similar manner to that described for the flat plate solution. Initial values at $\eta = 0$ for F_n'' , and T_n^{*} need to be obtained. This is done by iteratively solving the system of equations until the boundary conditions at $\eta = \infty$ are satisfied. To check the implementation of the solver, the obtained initial values are compared against those published by Goodrich[24] for a Prandtl number of 1. Table 4 shows the comparisons.

Table 4: Comparisons of the initial values for F_n'' , and T_n^{*} from the current study against those from Goodrich[24].

	F_0''	F_1''	F_2''	T_0^{*}	T_1^{*}	T_2^{*}
Goodrich [24]	0.6421	0.048035	-0.00195	-0.5671	-0.2237	0.0251
Present study	0.6421	0.04798	-0.00196	-0.5671	-0.2236	0.0252

Figure 15 shows the similarity comparison for temperature and velocity for a first rank heating rod. The flow at the rods is seen to agree quite well at $Z^* = 0.01$ but develops much faster compared to the containment wall and by $Z^* = 0.04$ it has largely deviated from the similarity solution. Temperature comparisons show quite good agreement at $Z^* = 0.01$, however even at $Z^* = 0.07$ there is just a slight deviation from the similarity solution.

3.4. Near-wall behaviour in the turbulent region

Non-dimensional near-wall profiles normalised using viscous wall units are presented in this section. The velocity profiles are normalised using the friction velocity (\bar{w}_τ) and plotted against the dimensionless distance (y^+) at Line_1 and Line_6. Friction velocity \bar{w}_τ is defined as $\sqrt{\tau_w}/\rho$, where the τ_w is the wall shear stress defined as $\mu d\bar{w}/dy|_{y=0}$. As to be expected for natural convective flows, the velocity profile deviates from the viscous sublayer profile ($\bar{w}^+ = y^+$) at $y^+ \approx 1$ and the log-law region typical to forced convection flows does not exist. Adopting the approach from

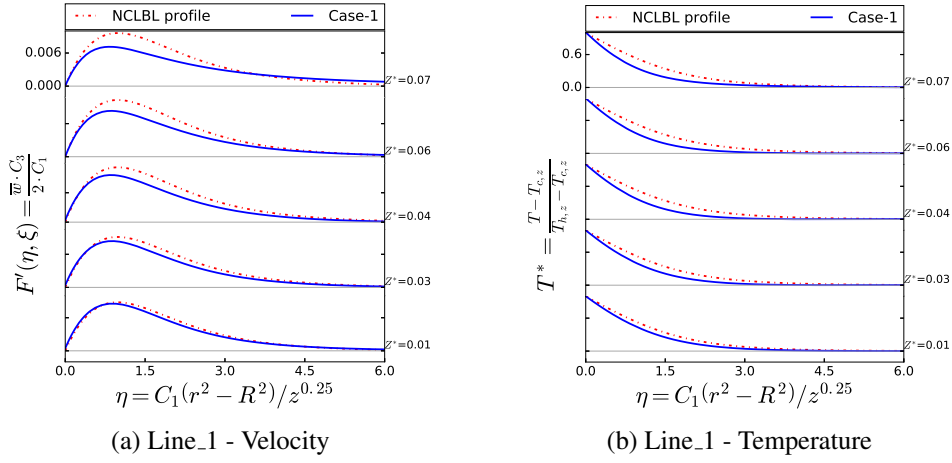


Figure 15: Temperature and Velocity comparison of LES simulation data against the slender cylinder similarity solution for Line_1. Data is extracted for the bottom region from $Z^* = 0.01$ to $Z^* = 0.07$. In the subfigures, $C_1 = Gr_{R,\Delta T_H}^{0.25} \left(R^{-7/4} / 2^{3/2} \right)$, $C_2 = Gr_{R,\Delta T_H}^{-0.25} \left(2^{3/2} / R^{1/4} \right)$ and $C_3 = Gr_{R,\Delta T_H}^{-0.75} \left(2^{3/2} / \nu R^{3/4} \right)$

525 Tsuji and Nagano[9], the inner layer is defined as the region from the peak of the profile to the wall. The outer layer is the region outside of this. The peaks for both lines are located between $y^+ = 20 - 30$. The profile for Line_1 at $Z^* = 0.8$ can be considered an outlier and peaks much closer to the wall at $y^+ \approx 10$, but this is likely due to the end effects as ascending flow is gradually arrested for example in the rectangular cavity by Barhaghi and Davidson[6], at $x/L = 0.9$ (close to
 530 the domain top end) the peak is closer to $y^+ = 10$. In Tsuji and Nagano's[9] experimental work the peaks were located around $y^+ = 30 - 40$ for the turbulent region and around $y^+ = 10 - 20$ for the laminar and transitional regions.

Profiles for Line_6 are largely self-similar below $Z^* = 0.6$. Compared to the profiles at $Z^* = 0.8$ and 0.9 (transitional and laminar flow), the peak values are much reduced with a broader region of
 535 occurrence. Looking at Line_1, the profiles are self-similar from $Z^* = 0.2$ to 0.6. The y^+ location of the peaks and the distribution for Line_6 is largely the same as that for Line_1. Although not shown, it should be noted the velocity profiles do not depend on *Grashof* number in the turbulent regions (away from the end effects). The peak values are much higher at the containment

than at the rods and the developed Line_6 profile at $Z^* = 0.5$ imposed onto Figure 16(a) clearly
 540 demonstrates this, however the inner layer is reasonably similar. Earlier contours and global line
 plots have shown remarkable differences between the flow profiles for Line_1 and Line_6, but as
 seen and discussed here the near-wall behaviour is largely as expected for natural convective flows.

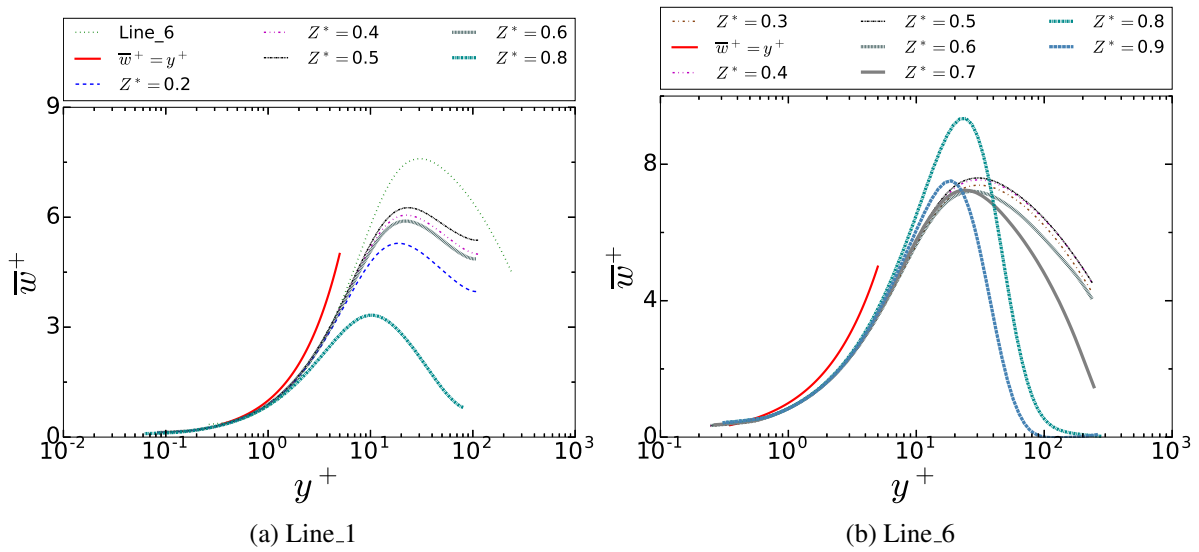


Figure 16: Non-dimensional near-wall profiles for \bar{w}^+ . Data is extracted from Case-1. In subfigure (a), Line_6 refers to the developed profile at $Z^* = 0.5$ taken from Line_6. The limits of the profiles in y/y_{max} units is 0.5 and 0.2 for Line_1 and Line_6, respectively.

Figure 17 shows the plot for T^+ against y^+ . The Line_1 profiles are almost identical at $Z^* = 0.4$
 and 0.5, and have a degree of similarity along other lines as well. For Line_6, the profiles are
 545 identical from $Z^* = 0.7$ and below. Near the wall a constant heat flux region is present and can
 be represented by the profile $T^+ = Pr y^+$. For both lines, departure from the profile ($T^+ = Pr y^+$)
 occurs at $y^+ \approx 6$. Looking at Figure 17, the developed profile from Line_6 at $Z^* = 0.5$ is nearly
 the same with the profiles for Line_1 at $Z^* = 0.4$ and 0.5.

Streamwise normal stress profiles plotted against y^+ are presented in Figure 18. Profiles for
 550 Line_1 show a degree of similarity from $Z^* = 0.2$ to 0.6. Interestingly, the peaks for Line_1
 also occur on the bounds of the inner layer $y^+ = 20 - 30$. In the flat vertical plate studies by

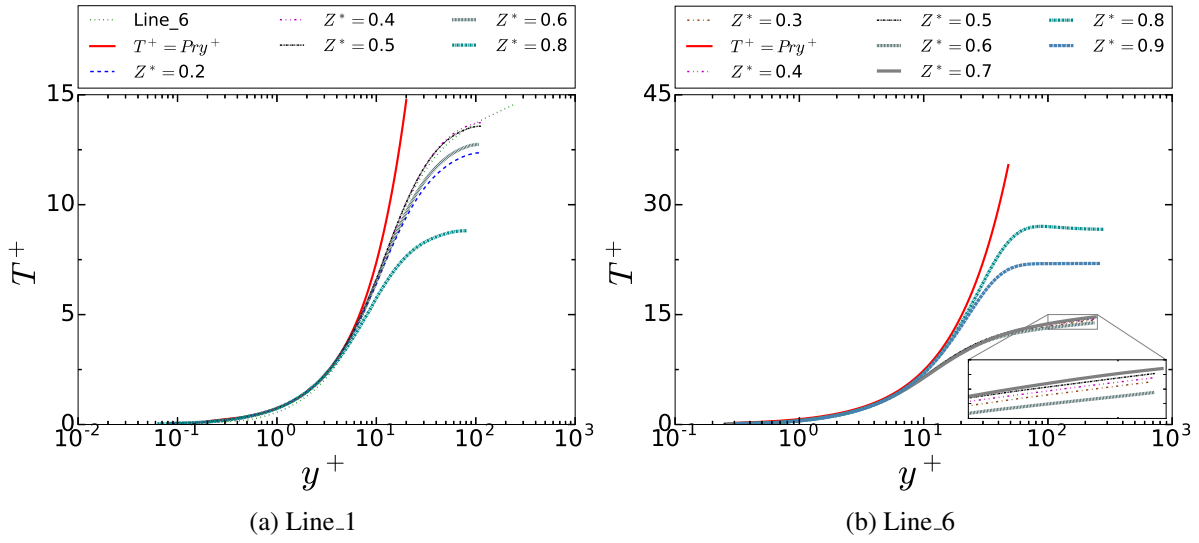


Figure 17: Non-dimensional near-wall profiles for T^+ . Data is extracted from Case-1. In subfigure (a), Line_6 refers to the developed profile at $Z^* = 0.5$ taken from Line_6. The limits of the profiles in y/y_{max} units is 0.5 and 0.2 for Line_1 and Line_6, respectively.

Nakao et al.[18] and Tsuji and Nagano[9], the peaks occurred past $y^+ = 100$, so well within the outer layer. The streamwise stress profiles for the square cavity by Sebilliau et al.[7] had peaks within the $y^+ = 10 - 100$ range. The variation was largely dependant on development distance and the Rayleigh number. For Line_6, where the flow is descending downwards; the boundary layer development to the fully turbulent condition is evident with reasonably self-similar profiles between $Z^* = 0.6 - 0.3$. The first near-wall peak for this line is around $y^+ = 40$ but turbulence is seen to increase again well past $y^+ = 100$ in some profiles. The peak value increases slightly from $Z^* = 0.9$ to $Z^* = 0.4$. Below this ($Z^* = 0.3$), the peak value reduces with increasing development length.

In Figure 19, the turbulent heat flux for the streamwise direction is shown. As can be seen, the peaks for both lines largely coincide with those from the velocity profiles (see Figure 16). This is largely consistent with the flat plate observations from Tsuji and Nagano[9] and the 5:1 cavity observations from Barhaghi and Davidson[6].

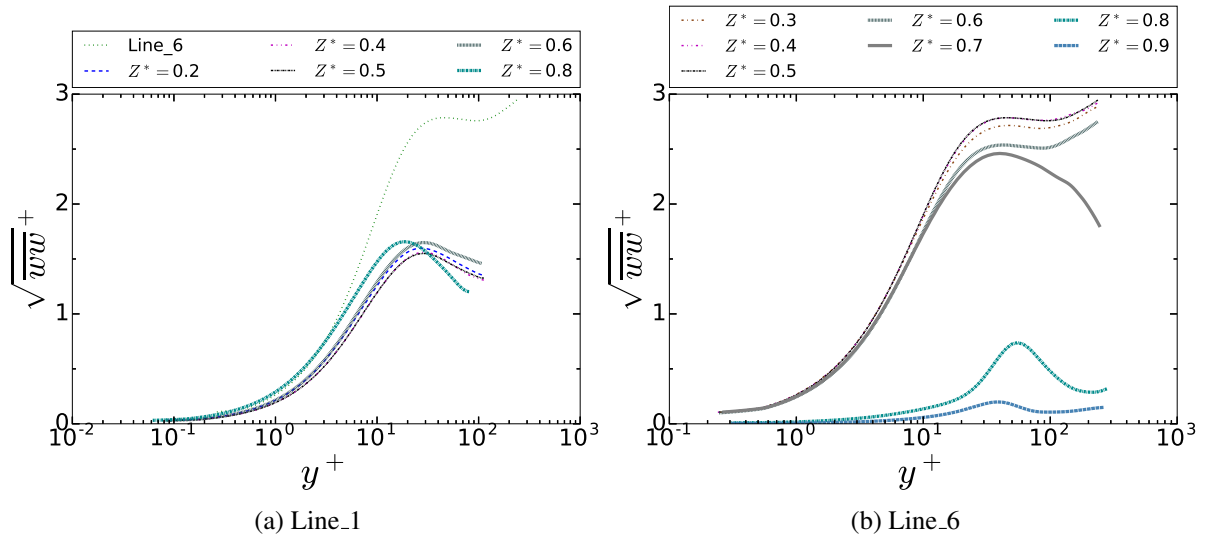


Figure 18: Non-dimensional near-wall profiles for the streamwise velocity fluctuation \overline{ww}^+ . Data is extracted from Case-1. In subfigure (a), Line_6 refers to the developed profile at $Z^* = 0.5$ taken from Line_6. The limits of the profiles in y/y_{max} units is 0.5 and 0.2 for Line_1 and Line_6, respectively.

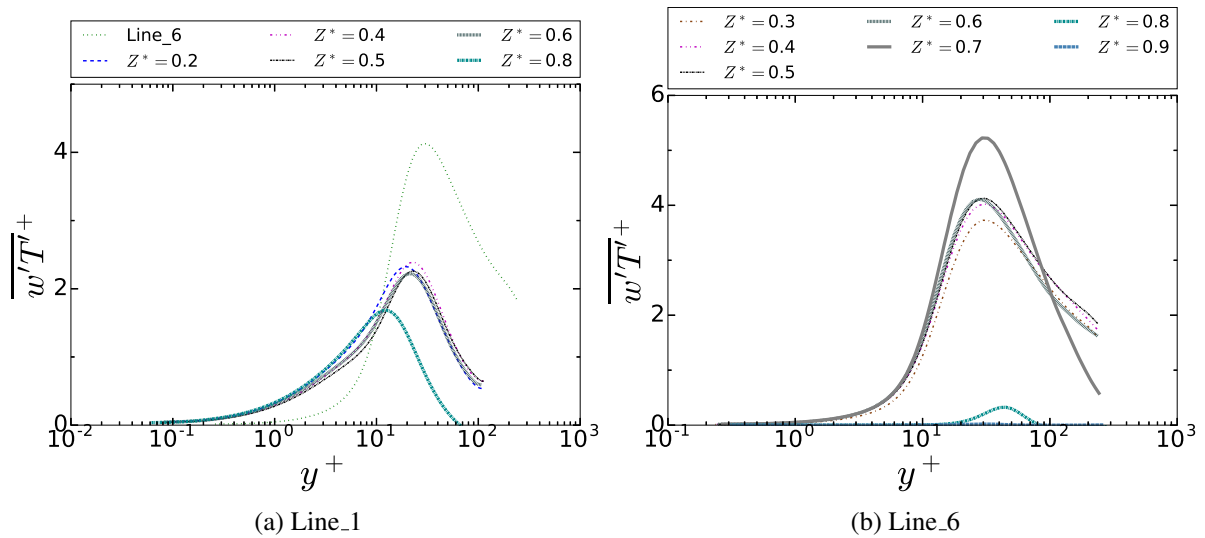


Figure 19: Non-dimensional near-wall profiles for the streamwise turbulent heat flux. Data is extracted from Case-1. In subfigure (a), Line_6 refers to the developed profile at $Z^* = 0.5$ taken from Line_6. The limits of the profiles in y/y_{max} units is 0.5 and 0.2 for Line_1 and Line_6, respectively.

565 Figure 20 shows the wall-normal component of the turbulence shear stress profiles \overline{rw}^+ . Close to the wall, these profiles exhibit a region of almost zero turbulence shear stress. For Line_6 (at containment wall) this region extends up to $y^+ \approx 15$, while for Line_1 (at rods) it extends up

to $y^+ \approx 3 - 6$. At the containment wall, this behaviour is largely expected with experimental flat plate results from Tsuji and Nagano[25] and LES results from Nakao et al.[18] showing this region extending to similar y^+ values. The LES results from Nakao et al.[18] are also particularly interesting as they show a slightly negative turbulent shear stress levels $y^+ \approx 8$. At the rods, this region is much shorter likely due to the effects of rod curvature. Line_6 also shows at $Z^* = 0.7$, within the transition region, the peak occurs at $y^+ \approx 150$. However, in the turbulent region, the peak is much higher and occurs at $y^+ > 500$. The changes in the turbulent region are related to the shear layer, which forms between the ascending and descending flows.

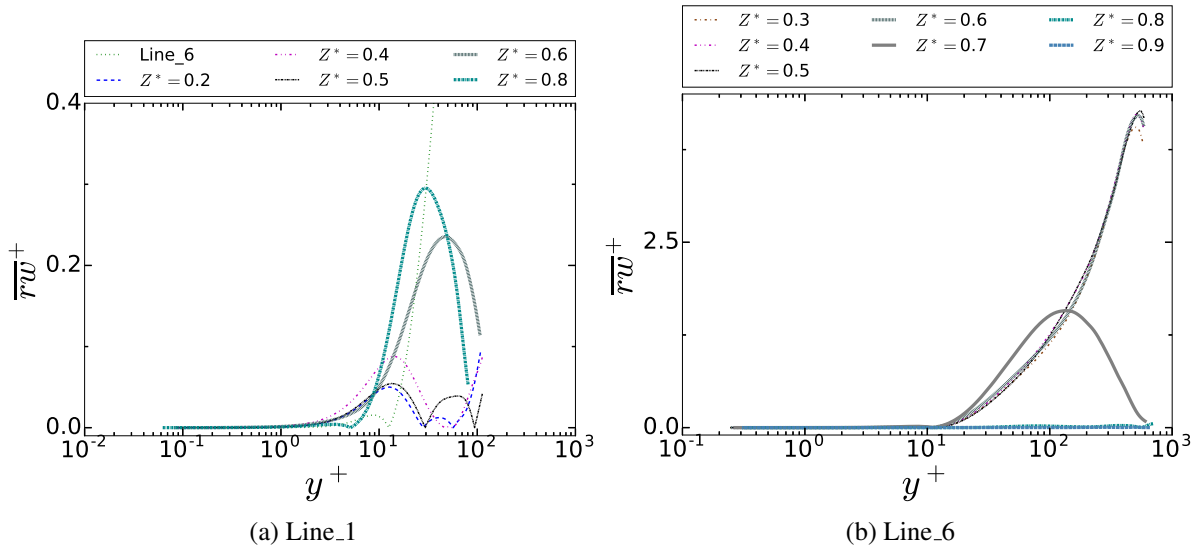


Figure 20: Non-dimensional near-wall profiles for the wall-normal turbulent shear stress. Data is extracted from Case-1. In subfigure (a), Line_6 refers to the developed profile at $Z^* = 0.5$ taken from Line_6. The limits of the profiles in y/y_{max} units is 0.5 and 0.4 for Line_1 and Line_6, respectively. To obtain, these profiles the wall-normal component of the turbulent shear stress τ_w^+ is computed by applying a tensor transformation along the extraction line.

3.5. Nusselt and friction factor at the containment surface

At the containment surface, the flow transitions from an initially laminar top-end to fully developed turbulence in the middle region. Correlations on this surface are given for the Nusselt number and friction factor coefficient in Figure 21.

There is a clear sudden increase in the Nusselt number indicating a transition to turbulence. The point of transition based on the Rayleigh number differs between the two heating cases; Case-1 transitions at 1.5×10^{10} and Case 2 at 6×10^9 . These transition Rayleigh numbers are significantly higher than that of natural convection over a vertical plate at $Ra_{cr} = 8 \times 10^8$ [9]. The Nusselt values for the laminar and turbulent regions are well represented by the correlations in Equation 15a and Equation 15b, respectively.

$$Nu_z = 0.5Ra_{z,\Delta T_H}^{0.25} \quad (15a)$$

$$Nu_z = 0.16Ra_{z,\Delta T_H}^{0.33} \quad (15b)$$

580 Assuming a flat vertical surface the exponent for the Nusselt number as a function of $Ra_{z,\Delta T}$ is 0.25 and 0.33 for laminar and turbulent flow, respectively[9]. The similarity of the exponents computed in the present study to those for a flat plate indicates the physical mechanisms are quite the same.

Figure 21 presents the friction factor coefficient against the Grashof number. Correlations for the laminar and turbulent region are given in Equation 16a and Equation 16b, respectively.

$$\frac{\tau_w}{\rho V_{n,\Delta T_H}^2} = 1.17Gr_{z,\Delta T_H}^{0.08} \quad (16a)$$

$$\frac{\tau_w}{\rho V_{n,\Delta T_H}^2} = 11.2Gr_{z,\Delta T_H}^{-0.025} \quad (16b)$$

Comparing against the results from Tsuji and Nagano[9], the laminar correlation is in good agreement to their given exponent of 0.0833. However, in the turbulent region their exponent was 0.084,
 585 while that in the present study is -0.025 . At the top region, the flow develops from a standing start thus with an increase of the local Grashof number ($Gr_{z,\Delta T_H}$) the friction factor also increases. This initial development is akin to that of a flat vertical plate, which is to be expected based on

the good comparisons against the flat plate similarity solution observed earlier. However, once the boundary layer transitions and develops there is a deviation from the flat plate behaviour to that resembling channel flow.

590

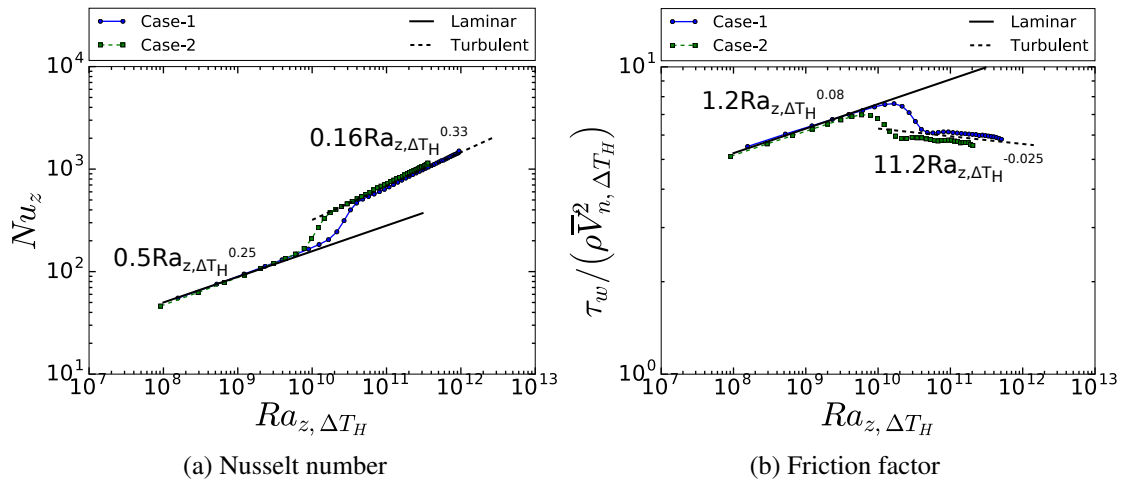


Figure 21: Nusselt number and friction factor plotted against the Rayleigh and Grashof number, respectively at the containment wall.

3.6. Sub-channel and bulk behaviour of the flow

Within this section, the domain is split into sub-channels as done in typical engineering analysis. Multiple cross-sections in the axial direction are extracted and using the sub-channels divisions given in Figure 2, the mass flow, fluid bulk temperature and solid temperature are computed.

595

Figure 22 shows the sub-channel mass flow variation. Below $Z^* = 0.8$, the mass flow is significantly altered; the mass flow in the interior sub-channels decreases significantly and the reverse happens for the exterior sub-channels (7, 8 & 9). At this location, transition at the containment surface occurs. As shown earlier in the contour plots, a strong cross-flow forms as the coolant is entrained towards the containment wall increasing the mass flow for the sub-channels there. The

600

fluid and sub-channel average solid temperature variations are presented in Figure 23. At the top-end where the temperature field is stratified, the gradient is significantly steeper. In the turbulent

region, the vertical temperature gradient is much shallower and almost flat. The sub-channel fluid temperature shows above $Z^* = 0.8$, there is a clear separation between the exterior and interior sub-channels. However, in the turbulent region, the separation between the exterior and interior sub-channels is non-existent. The sub-channel average solid temperatures largely follow the vertical temperature gradient changes observed for the fluid and they do not show a significant variation between the sub-channels.

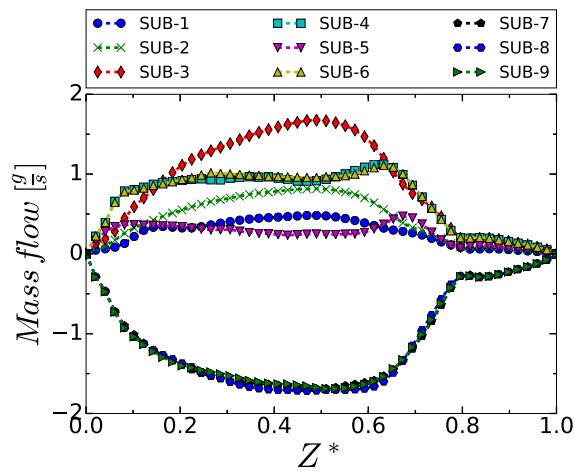


Figure 22: Variation of the sub-channel mass flow as a function of height.

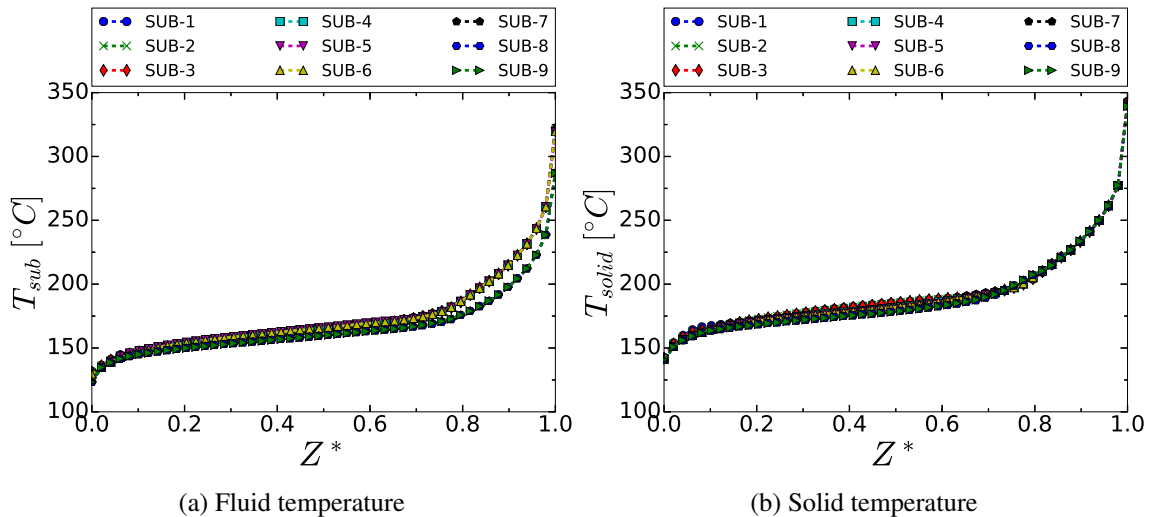


Figure 23: Sub-channel solid and fluid temperature variation with height.

Vertical planes connecting rods of the same ranks at the azimuthal rod gap spaces are used to compute the lateral mixing between the sub-channels at the different radii. Line_1 is an example of such a plane. In total six such planes are extracted and then split into fifty axial sections. The variables required are then computed normal to the plane (radial direction) of interest.

The radial mass flow is given in Figure 24. Immediately after transition at the containment surface, there is a sudden increase in mass transfer from the interior to exterior sub-channels. This corroborates the axial mass flow plots seen earlier.

Peak levels of radial mass transfer are observed across the third rank rod gaps. This is due to their proximity to the containment surface and also the cumulative effect of the mass transfer from the first and second rank rod gaps. At $Z^* = 0.5$, the radial transfer to the containment has subsided and the net lateral flow direction shifts towards the interior. Mass transfer towards the interior does gradually increase as the flow descends, with peaks being observed at the bottom-end.

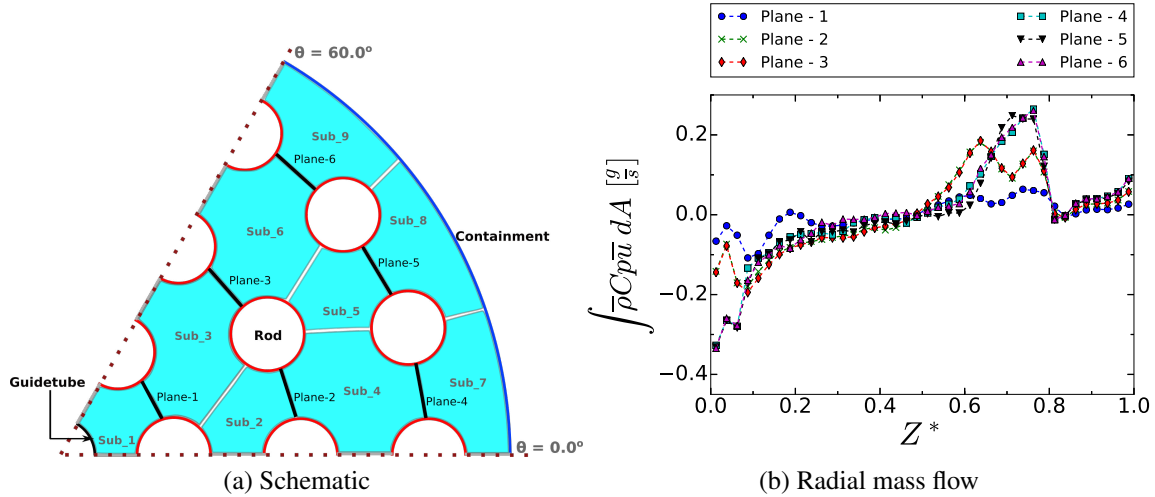


Figure 24: Radial mass flow variation through the rod gaps. A positive value means transfer is directed towards the containment surface. Subfigure (a) shows the location of the extraction planes.

Figure 25 shows the heat flow as a result of convection and turbulence mixing. As to be expected, the heat convected largely follows the observations and trends noted for the lateral mass

flow. On the other hand turbulent mixing peaks close to the domain mid-height and accounts for a much smaller portion of the heat transfer.

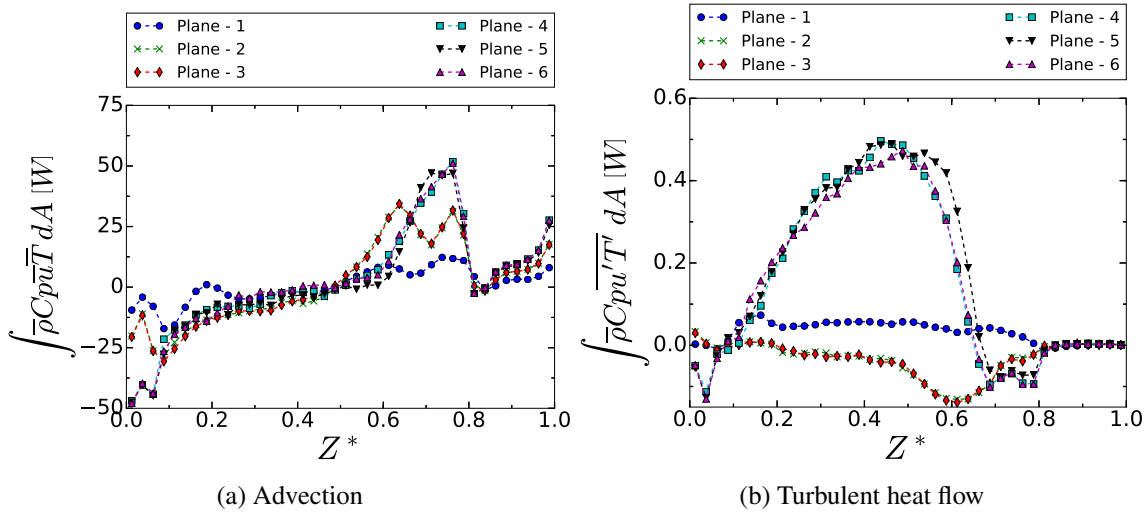


Figure 25: Radial advection and turbulent heat flow through the rod gaps. Subfigure 24(a) shows the location of the extraction planes.

4. Conclusions

625 Natural circulation simulations in a turbulent enclosed rod bundle cavity of large aspect ratio have been carried out. It has been shown the cavity can be split into three distinct vertical regions, simply termed the top ($Z^* > 0.75$), middle ($0.15 < Z^* < 0.75$), and bottom ($Z^* < 0.15$). The axial extent of these regions is mostly dependent on the flow condition at the containment wall. A laminar boundary layer flow regime at the containment wall coupled with turbulent boundary layer
630 flow at the rod walls defines the top region. In the core of this region, the temperature is heavily stratified. Laminar correlations for Nusselt number and friction factor at the containment wall are similar to those for natural convection on a flat vertical surface with dependences of $0.5Ra_{z,\Delta T_H}^{0.25}$ and $1.17Gr_{z,\Delta T_H}^{0.08}$. This indicates laminar flow and thermal development at this surface is not dissimilar from an isolated vertical surface. Comparisons with the natural convection flat plate similarity

635 solution by Ostrach[21] further confirmed this.

The middle region encompasses most of the domain, and the flow here is particularly complex and dominated by turbulence effects. Flow at the containment, transitions to turbulence thereby instigating entrainment from the interior sub-channels (at transition location), which is then followed by strong mixing. In this region, the resulting vertical temperature distribution is uniform.

640 The middle region was further split into two parts; the outer region which is between the second rank rods and containment wall and a central region which is between the adiabatic central rod and heating second rank rod. The outer region, is akin to a heating and cooling “channel”, with a strong shear layer as the opposing upward interior flow and large scale downward flow at the containment interact. This can be linked to the highly turbulent Betts and Bokhari[4] case study. Heated down-

645 ward flow is shown to exist at the third rank rod surfaces, which are closest to the containment wall. The central region is typical of a heated upward flow but with strong interference from the outer region leading to mixed/forced convection like profiles across the gaps. Observations have shown the chimney effect occurs to some extent in this “channel”. Although flow profiles show a stark difference between the outer and central regions, their near-wall behaviour has the typical

650 characteristics of natural convective flows. Turbulent correlations for Nusselt number over the containment wall have a Rayleigh number dependency of $0.16Ra_{z,\Delta T_H}^{0.33}$, which is similar to that for a vertical plate. However, for the friction factor, the correlation has a Grashof number dependency of $11.2Gr_{z,\Delta T_H}^{-0.025}$, and hence has an exponent that is very different from that for a flat plate (at 0.084) from the Tsuji and Nagano case study[9].

655 The bottom region is characterised by a downward flow impinging onto the floor at the containment wall. Boundary layer development occurs at the rod surfaces as the flow begins its upward ascent. The comparison of the velocity from simulations against the slender cylinder similarity laminar solution shows transition occurs much faster here than on the containment wall.

Acknowledgements

660 This work is supported through a studentship provided by EDF energy and has been performed using resources provided by the Cambridge Tier-2 system funded by EPSRC Tier-2 capital grant EP/P020259/1.

Appendix

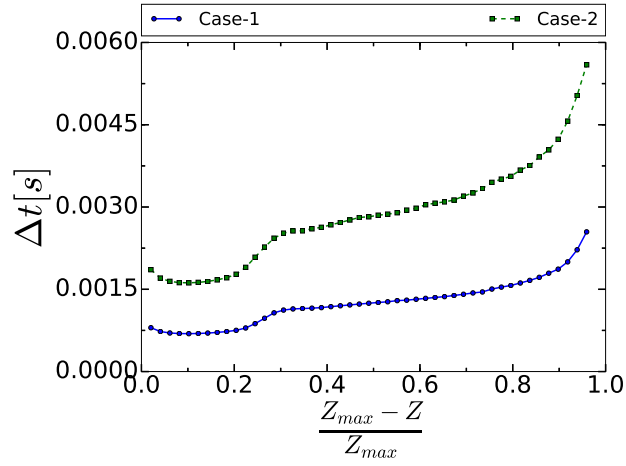


Figure A1: Profiles of the wall time step along the containment wall generated for case-1 and case-2. The 0 location is the top of the containment wall.

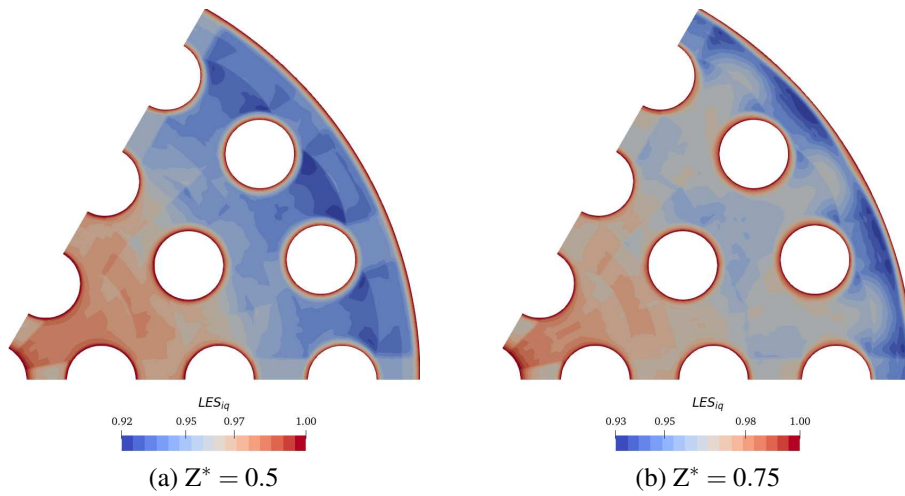


Figure A2: Contours of the LES_IQ parameter at varying heights and taken from the highest heating case. The scalebar is reset at each axial location to maximise the variation. LES is considered to be good if the values obtained are $LES_IQ > 0.8$.

References

665 [1] J. W. Elder, Turbulent free convection in a vertical slot, *Journal of Fluid Mechanics* 23 (1) (1965) 99–111.

doi:10.1017/S0022112065001246.

- [2] S. Yin, T. Wung, K. Chen, Natural convection in an air layer enclosed within rectangular cavities, *International Journal of Heat and Mass Transfer* 21 (3) (1978) 307–315. doi:10.1016/0017-9310(78)90123-0.
URL <https://www.sciencedirect.com/science/article/pii/0017931078901230>
- 670 [3] R. K. MacGregor, A. F. Emery, Free Convection Through Vertical Plane Layers—Moderate and High Prandtl Number Fluids, *Journal of Heat Transfer* 91 (3) (1969) 391–401. doi:10.1115/1.3580194.
- [4] P. Betts, I. Bokhari, Experiments on turbulent natural convection in an enclosed tall cavity, *International Journal of Heat and Fluid Flow* 21 (6) (2000) 675–683. doi:10.1016/S0142-727X(00)00033-3.
URL <https://www.sciencedirect.com/science/article/pii/S0142727X00000333>
- 675 [5] K. Cheesewright, K. King, S. Ziai, Experimental data for the validation of computer codes for the prediction of two-dimensional buoyant cavity flows, in: *ASME Winter Annual Meeting*, ASME, Anaheim, 1986, pp. 75–81.
- [6] D. G. Barhaghi, L. Davidson, Natural convection boundary layer in a 5:1 cavity, *Physics of Fluids* 19 (12) (2007) 1–16. doi:10.1063/1.2815746.
- [7] F. Sebilleau, R. Issa, S. Lardeau, S. P. Walker, Direct Numerical Simulation of an air-filled differentially heated square cavity with Rayleigh numbers up to 10^{11} , *International Journal of Heat and Mass Transfer* 123 (2018) 297–319. doi:10.1016/J.IJHEATMASSTRANSFER.2018.02.042.
680 URL [#}f0005">https://www.sciencedirect.com/science/article/pii/S0017931018302588{#}f0005](https://www.sciencedirect.com/science/article/pii/S0017931018302588)
- [8] D. Kizildag, F. Trias, I. Rodríguez, A. Oliva, Large eddy and direct numerical simulations of a turbulent water-filled differentially heated cavity of aspect ratio 5, *International Journal of Heat and Mass Transfer* 77 (2014) 1084–1094. doi:10.1016/J.IJHEATMASSTRANSFER.2014.06.030.
685 URL <https://www.sciencedirect.com/science/article/pii/S001793101400502X>
- [9] T. Tsuji, Y. Nagano, Characteristics of a turbulent natural convection boundary layer along a vertical flat plate, *International Journal of Heat and Mass Transfer* 31 (8) (1988) 1723–1734. doi:10.1016/0017-9310(88)90284-0.
690 URL <https://www.sciencedirect.com/science/article/pii/0017931088902840>
- [10] E. R. G. Eckert, A. Diaguila, Experimental investigation of free-convection heat transfer in vertical tube at large Grashof numbers, Tech. rep., National Advisory Committee for Aeronautics, Washington (1952).
- [11] W. M. Yan, T. F. Lin, Theoretical and experimental study of natural convection pipe flows at high Rayleigh number, *International Journal of Heat and Mass Transfer* 34 (1) (1991) 291–303. doi:10.1016/0017-9310(91)90195-K.
695

- [12] S. M. Ohk, B. J. Chung, Natural convection heat transfer inside an open vertical pipe: Influences of length, diameter and Prandtl number, *International Journal of Thermal Sciences* 115 (2017) 54–64. doi:10.1016/j.ijthermalsci.2017.01.014.
URL <http://dx.doi.org/10.1016/j.ijthermalsci.2017.01.014>
- 700 [13] T. Inagaki, S. Maruyama, Turbulent heat transfer of natural convection between two vertical parallel plates, *Heat Transfer - Asian Research* 31 (1) (2002) 56–67. doi:10.1002/htj.10017.
- [14] W. M. Lewandowski, M. Ryms, H. Denda, Natural convection in symmetrically heated vertical channels, *International Journal of Thermal Sciences* 134 (2018) 530–540. doi:10.1016/J.IJTHERMALSCI.2018.08.036.
URL <https://www.sciencedirect.com/science/article/pii/S1290072917317453>
- 705 [15] M. Keyhani, F. A. Kulacki, R. N. Christensen, Experimental investigation of free convection in a vertical rod bundle—a general correlation for nusselt numbers, *Journal of Heat Transfer* 107 (3) (1985) 611–623. doi:10.1115/1.3247468.
- [16] K. Chinembiri, J. Li, S. He, C. Trinca, Natural circulation in a short enclosed rod bundle (submitted), *International Journal of Heat and Mass Transfer* (2021) 1–20.
- 710 [17] F. Nicoud, F. Ducros, Subgrid-scale stress modelling based on the square of the velocity, *Agricultural Economics Research Review* 19 (2006) 37–48. arXiv:arXiv:1503.01439v1, doi:10.1016/j.jcp.2004.10.018.
- [18] K. Nakao, Y. Hattori, H. Suto, Numerical investigation of a spatially developing turbulent natural convection boundary layer along a vertical heated plate, *International Journal of Heat and Fluid Flow* 63 (2017) 128–138. doi:10.1016/J.IJHEATFLUIDFLOW.2016.09.006.
URL <https://www.sciencedirect.com/science/article/pii/S0142727X16305501>
- 715 [19] E. Lemmon, M. Huber, M. McLinden, NIST Standard Reference Database 23: Reference Fluid Thermodynamic and Transport Properties (REFPROP), Version 9.0. (2010).
- [20] I. B. Celik, Z. N. Cehreli, I. Yavuz, Index of resolution quality for large eddy simulations, *Journal of Fluids Engineering, Transactions of the ASME* 127 (5) (2005) 949–958. doi:10.1115/1.1990201.
- 720 [21] S. Ostrach, An analysis of laminar free-convection flow and heat transfer about a flat plate parallel to the direction of the generating body force, Tech. rep., National Advisory Committee for Aeronautics, Cleveland (1952). arXiv:arXiv:1011.1669v3, doi:10.1017/CB09781107415324.004.
- [22] C. O. Popiel, Free convection heat transfer from vertical slender cylinders: A review, *Heat Transfer Engineering* 29 (6) (2008) 521–536. doi:10.1080/01457630801891557.

- 725 [23] E. Sparrow, J. Gregg, Laminar free convection from a vertical plate with uniform surface heat flux, in: ASME
78, 1956, pp. 435 – 440.
- [24] S. S. Goodrich, Natural convection heat transfer and boundary layer transition for vertical heated cylinders,
Ph.D. thesis, Oregon State University (2017).
- [25] T. Tsuji, Y. Nagano, Turbulence measurements in a natural convection boundary layer along a vertical flat plate,
730 International Journal of Heat and Mass Transfer 31 (10) (1988) 2101–2111. doi:10.1016/0017-9310(88)
90120-2.